Heterogeneous Synaptic Homeostasis: A Novel Mechanism Boosting Information Propagation in Neural Circuitry

Farhad Razi[1,✉] **and Belén Sancristóbal**[2]

[1]Center for Brain and Cognition, Universitat Pompeu Fabra, Ramón Trias Fargas, Barcelona, 08018, Catalonia, Spain
[2]Barcelona School of Design and Engineering, Universitat de Vic—Universitat Central de Catalunya, La Rambla, Barcelona, 08002, Catalonia, Spain

Behavioral responses to auditory stimuli decrease from wakefulness to deep phases of sleep. This reduction in behavioral responses can be attributed to the diminished efficiency of neural communications within the cerebral cortex. Substantial experimental evidence underscores that the spatiotemporal spread of neural responses to external stimuli within the cerebral cortex is more extensive during wakefulness compared to deep sleep. However, the fundamental neural mechanisms driving this phenomenon remain unclear. One potential candidate is synaptic upscaling of cortical excitatory connections during wakefulness, aligning with the synaptic homeostasis hypothesis. Nonetheless, we argue that a uniform synaptic upscaling in a balanced configuration, without overexcitation or overinhibition, during wakefulness is insufficient to explain this observation. Instead, we propose a hypothesis suggesting that synaptic upscaling during wakefulness should be heterogeneous to account for the heightened propagation of neural responses within the cerebral cortex. Specifically, we propose that the upscaling of excitatory connections between distinct cortical areas (inter-excitatory connections) should exceed that within each cortical area (intra-excitatory connections). To explore this hypothesis, we utilized a computational model of coupled cortical columns. Our findings reveal that synaptic upscaling during wakefulness introduces a dynamic interplay between inter- and intra-excitatory connections. Synaptic upscaling of inter-excitatory connections enhances the propagation of information content and neural responses to external inputs, while the synaptic upscaling of intra-excitatory connections has a diminishing effect. Our computational results suggest that synaptic upscaling during wakefulness should be heterogeneous, favoring inter-excitatory connections over intra-excitatory connections. This heterogeneity is crucial for facilitating the propagation of information content and neural responses across distinct cortical areas during wakefulness compared to deep sleep.

cortical effective connectivity | heterogeneous synaptic homeostasis | information propagation | wakefulness | NREM sleep

Correspondence: ***farhad.razi.1988@gmail.com***

Introduction

Mounting evidence suggests that the capacity of the cerebral cortex to transmit neural responses across distributed cortical areas, referred to as cortical effective connectivity (1), is heightened during wakefulness compared to deep phases of sleep, also known as non-rapid eye movement (NREM) sleep (2–4). Yet, the precise neural mechanisms underlying this enhanced propagation of neural responses within the cerebral cortex remain largely mysterious.

In general, the changes in propagation patterns of neural responses can be attributed to alterations in synaptic and/or neuronal dynamics within the neural pathways integral to transmitting neural responses. The silent neuromodulatory milieu during sleep (5) changes the synaptic dynamics by suppressing cellular markers of synaptic upscaling across various brain regions, potentially contributing to the well-established challenges associated with memory acquisition during sleep (6). Furthermore, it changes the neuronal dynamics by alternating neuronal activity between active (Up) and silent (Down) states during NREM sleep (7, 8). These alternations in neuronal activity during NREM sleep potentially contribute to the large–amplitude–low–frequency signals, also known as slow wave activity (SWA), in electroencephalography (EEG) (9) and local field potential (LFP) (10) recordings.

The prevailing scientific view attributes the distinct patterns of response propagation in the cerebral cortex solely to changes in the dynamics of cortical neurons during the shift from wakefulness to NREM sleep, while downplaying the role of changes in the dynamics of cortical synaptic strength (11–14). According to this perspective, cortical neurons tend to enter evoked Down states following external perturbations, disrupting long-lasting causal interactions among cortical areas during NREM sleep. However, to the best of our knowledge, direct experimental evidence supporting this claim remains elusive, and certain empirical observations raise questions about the adequacy of changes in neuronal dynamics as the sole explanation.

For instance, Pigorini et al. reported a correlation between the amplitude of evoked SWA, a proxy for evoked Down states, and the disruption of causal cortical interactions (14). However, they also reported that causal interactions persisted longer during wakefulness compared to NREM sleep in cortical areas adjacent to the stimulation site, despite similar levels of evoked SWA during both states. Accordingly, it remains unclear why similar levels of evoked SWA during wakefulness were insufficient to disrupt the causal interactions in those areas. Furthermore, studies involving single- and multi-unit recordings from the primary auditory cortex (A1) in monkeys (15), rats (16, 17), and humans (4) have demonstrated that evoked neural responses to auditory stimuli is preserved despite the shift in neural dynam-

DRAFT

ics from NREM sleep to wakefulness. It is only in higher-order cortical areas downstream from A1 that evoked neural responses are enhanced during wakefulness compared to NREM sleep (4, 17). These observations suggest that the change in the neuronal dynamics alone cannot entirely account for the different response propagation patterns in the cerebral cortex and open the possibility that changes in synaptic dynamics should also influence the response propagation patterns.

A potential neural correlate of alterations in synaptic dynamics may involve the upscaling of cortical excitatory connections during wakefulness compared to NREM sleep, in line with the synaptic homeostasis hypothesis (SHY) (18, 19). SHY posits that synaptic strength in many cortical circuits decreases during sleep to offset the net synaptic upscaling that occurs during wakefulness. Synaptic upscaling during wakefulness has the potential to amplify evoked (stimuli-relevant) postsynaptic currents. Given the larger projecting axons of excitatory neurons compared to the more localized axons in inhibitory neurons (20–22), synaptic upscaling can consequently increase the amplitude of evoked neural responses in a hierarchical cortical processing chain. This mechanism exerts a *driving effect* on transmission of neural responses across different cortical areas.

However, it is essential to note that synaptic upscaling also elevates spontaneous (stimuli-irrelevant) postsynaptic currents. *In vitro* studies have demonstrated that an increase in spontaneous synaptic currents, in a balanced configuration without overexcitation or overinhibition, decreases the amplitude of evoked neural responses to external inputs (23). Considering that changes in excitation and inhibition often co-occur in neural circuits (24), the increase in excitatory synaptic currents during wakefulness due to synaptic upscaling should be paralleled by an increase in inhibitory synaptic currents. This results in an elevation in spontaneous synaptic currents in a balanced configuration. Therefore, synaptic upscaling during wakefulness increases spontaneous synaptic currents, which can potentially reduce the amplitude of evoked neural responses. This mechanism exerts a *pulling effect* on transmission of neural responses across different cortical areas.

In light of these considerations, we propose a hypothesis that synaptic upscaling during wakefulness initiates a competition between two opposing forces: the driving and pulling effects. A uniform synaptic upscaling during wakefulness, without selectivity favoring the driving effect over the pulling effect, may not suffice to explain the enhanced propagation of neural responses during wakefulness compared to NREM sleep.

Within a hierarchical model of cerebral cortex (25, 26), excitatory connections can be categorized into two types: excitatory connections between cortical areas (inter-excitatory connections) and excitatory connections within each cortical area (intra-excitatory connections). The former category represents a class of driver synaptic connections responsible for hierarchically transmitting neural responses, while the latter signifies modulatory synaptic connections regulating neural responses. During wakefulness within a cortical area, inter-synaptic upscaling amplifies stimulus-relevant postsynaptic currents, resulting in the driving effect. Conversely, intra-synaptic upscaling enhances spontaneous postsynaptic currents, resulting in the pulling effect. Therefore, we propose that synaptic upscaling should be heterogeneous at the circuit level in a hierarchical cortical processing chain, favoring inter- over intra-synaptic upscaling, to ensure the driving effect prevails over the pulling effect. We term this hypothesis *heterogeneous synaptic homeostasis*.

To assess our hypothesis, which poses significant challenges for current experimental methods, we employed the computational Wilson–Cowan neural mass model (27), designed to simulate the average firing rate signal of a cortical column (referred to as the one-cortical-column model). This model was adapted to replicate NREM- and wakefulness-like dynamics (28). Initially, we replicated our previous findings (29), demonstrating that synaptic upscaling of intra-excitatory connections (by a factor of β_{intra}) in a balanced configuration (augmenting inhibition to counteract overexcitation) was sufficient to shift the spontaneous activity of the model from NREM-like to wakefulness-like dynamics.

To illustrate the modulation of synaptic upscaling of intra- and inter-excitatory connections (by a factor of β_{intra} and β_{inter}, respectively) on evoked neural responses, we examined responses of the one-cortical-column model to inputs applied through inter-excitatory connections. Subsequently, we expanded the model to encompass two symmetric cortical columns (referred to as the two-cortical-column model), interconnected by inter-excitatory connections. Within this setup, one of the columns (referred to as the perturbed cortical column) was directly subjected to inputs, while the other column (the unperturbed cortical column) received inputs indirectly via inter-excitatory connections originating from the perturbed to the unperturbed cortical column. We then assessed the modulation of intra- and inter-synaptic upscaling on propagation of neural responses from the perturbed to the unperturbed cortical column in the two-cortical-column model. Furthermore, we introduced a framework for quantifying information content in evoked neural responses. Through this framework, we examined how intra- and inter-synaptic upscaling impacted information content and its propagation. Our comprehensive computational approach aimed to shed light on the intricate interplay of synaptic upscaling forces and their contributions to the propagation of information and neural responses in neural circuitry.

Results

One-cortical-column model. The one-cortical-column model consists of one pyramidal and one inhibitory population (Fig. 1a). Our analysis were carried out on simulated firing rate signals from the pyramidal population.

Electrophysiological patterns. The one-cortical-column model produces electrophysiological patterns (Methods) associated with NREM sleep and wakefulness. When there is no intra-synaptic upscaling ($\beta_{\text{intra}} = 1$, Fig. 1b), firing rate signals from the pyramidal population in the model exhibit distinct characteristics of NREM sleep (for the parameter

DRAFT

set detailed in the Table 1,2): firing rate signals are characterized by (i) high amplitude, (ii) a bimodal distribution, and (iii) a greater power content in the lower-frequency component (Fig. 1c(i)-(iii)). These dynamical features are robust to the changes in the standard deviation of the noise in the model varied by 10% (Extended Data Fig. 1). However, intra-synaptic upscaling ($\beta_{\text{intra}} > 1$, Fig. 1b), in a balanced configuration (Methods and Table 3) gradually shifts the dynamics towards wakefulness (Extended Data Fig. 2), in line with SHY (18, 19). Intra-synaptic upscaling transforms the firing rate signals characterized by (i) low amplitude, (ii) a unimodal distribution, and (iii) a greater power content in the higher-frequency component (Fig. 1d(i)-(iii)). Moreover, the power ratio of slow oscillations in signals, the hallmark of NREM sleep, decreases with increasing intra-synaptic upscaling (Fig. 1e). These results demonstrate that the one-cortical-column model replicates well-established electrophysiological patterns of NREM sleep and wakefulness (7, 8, 10, 30–32).

Evoked responses to inputs. Inputs are applied through inter-excitatory connections to the one-cortical-column model (Fig. 2a), ranging from 10 Hz to 90 Hz in increments of 20 Hz (Methods). The inputs represents the strength of presynaptic firing of the pyramidal population in an upstream cortical area, which was not explicitly modeled. Given the presence of inter-excitatory connections, synaptic upscaling in wakefulness occurs in two directions: intra- and inter-synaptic upscaling (Fig. 2b). We evaluated evoked responses in the model, exploring various combinations of intra- and inter-synaptic upscaling parameters (Fig. 2b).

Noise-free evoked responses (Methods) exhibit distinct characteristics during NREM sleep ($\beta_{\text{intra}} = \beta_{\text{inter}} = 1$) and wakefulness ($\beta_{\text{intra}} > 1$ and $\beta_{\text{inter}} > 1$). In NREM sleep (when there is no synaptic upscaling), responses assume a slow wave shape, featuring an initial surge in firing rate above prestimulus values followed by a subsequent decrease that extends beyond the input offset (Fig. 2c(i)). This temporal pattern corresponds to poststimulus neuronal activation and subsequent suppression of neuronal activity. In contrast, during wakefulness, evoked responses exhibit an initial increase in firing rate, yet the subsequent suppression of neuronal activity either does not manifest or is notably diminished compared to that observed during NREM sleep (Fig. 2c(ii)). These findings corroborate earlier research by Nir and colleagues (16).

To evaluate quantitatively the effects of intra- and inter-synaptic upscaling on the evoked responses, our analysis were primarily carried out on the amplitude of evoked firing responses at the input offset. Detailed analysis of noise-free simulations further revealed that the amplitude of evoked responses increases with increasing input strength during NREM sleep and all synaptic upscalings in wakefulness (Fig. 2d(i)). Moreover, the amplitude of evoked responses is notably greater during NREM sleep in comparison to wakefulness. Interestingly increasing intra-synaptic upscaling (β_{intra}) during wakefulness, while inter-synaptic upscaling (β_{inter}) is constant, produces a distinct *pulling* effect that results in decreasing the amplitude of evoked responses (Fig. 2d(i)). It is important to note that spontaneous synaptic activity ($|\text{E}| + |\text{I}|$, Methods) increases with increasing intra-synaptic upscaling, which in turn decreases the amplitude of evoked neural responses to inputs (Extended Data Fig. 3a). These results corroborate the findings from *in vitro* studies (23).

Conversely, elevating inter-synaptic upscaling while holding intra-synaptic upscaling constant during wakefulness produces a distinct *driving* effect that results in increasing the amplitude of evoked responses (Fig. 2d(ii)). These results highlight that synaptic upscaling introduces a dynamic interplay between driving and pulling effects on shaping evoked responses during wakefulness. Given that inter-excitatory connections are dynamically implicated only during the transient input application, inter-synaptic upscaling does not modulate the spontaneous synaptic activity (Extended Data Fig. 3a). However, both intra and inter-synaptic upscalings increase the evoked synaptic excitation in response inputs. Nonetheless, it is inter-synaptic upscaling that increases the net evoked synaptic current ($\Delta\text{E}-\Delta\text{I}$, Methods), as opposed to when intra-synaptic upscaling increases in wakefulness (Extended Data Fig. 3b). This phenomena generates the dynamic interplay between driving and pulling effects for inter- and intra-excitatory connections.

We explored the three distinct configurations of synaptic upscaling in wakefulness (Fig. 2b): local-selective ($\mathbf{LS}: \beta_{\text{intra}} > \beta_{\text{inter}} > \mathbf{1}$), homogeneous ($\mathbf{H}: \beta_{\text{intra}} = \beta_{\text{inter}} > \mathbf{1}$), and distance-selective ($\mathbf{DS}: \beta_{\text{inter}} > \beta_{\text{intra}} > \mathbf{1}$). Organizing our results according to these configurations revealed that synaptic upscaling in wakefulness does not enhance the amplitude of evoked responses unless it selectively favors inter-synaptic upscaling over intra-synaptic upscaling (Fig. 2e and Extended Data Fig. 3c).

Subsequently, our study delved into the assessment of information content (Methods) in stochastic evoked firing responses. Information detection quantifies performance of an optimal classifier in distinguishing the distribution of evoked responses at the input offset to a given input strength from the distribution of spontaneous activities at a random time point in the prestimulus interval. On the other hand, information differentiation quantifies performance of an optimal classifier in distinguishing the distribution of evoked firing responses at the input offset for different input strengths.

Information detection during NREM sleep increases with increasing input strength (Fig. 3a), so does for all synaptic upscalings in wakefulness. Nonetheless, our results indicate that intra-synaptic upscaling during wakefulness produces a pulling effect decreasing information detection (Fig. 3a). On the other hand, inter-synaptic upscaling during wakefulness produces a driving effect enhancing information detection (Fig. 3a). Organizing the results according to the three synaptic upscaling configurations in wakefulness manifests that synaptic upscaling in wakefulness does not enhance information detection unless it occurs in a distance-selective manner (Fig. 3b and Extended Data Fig. 4). It is important to mention that evoked responses exhibited larger amplitudes during NREM sleep compared to synaptic upscal-

DRAFT

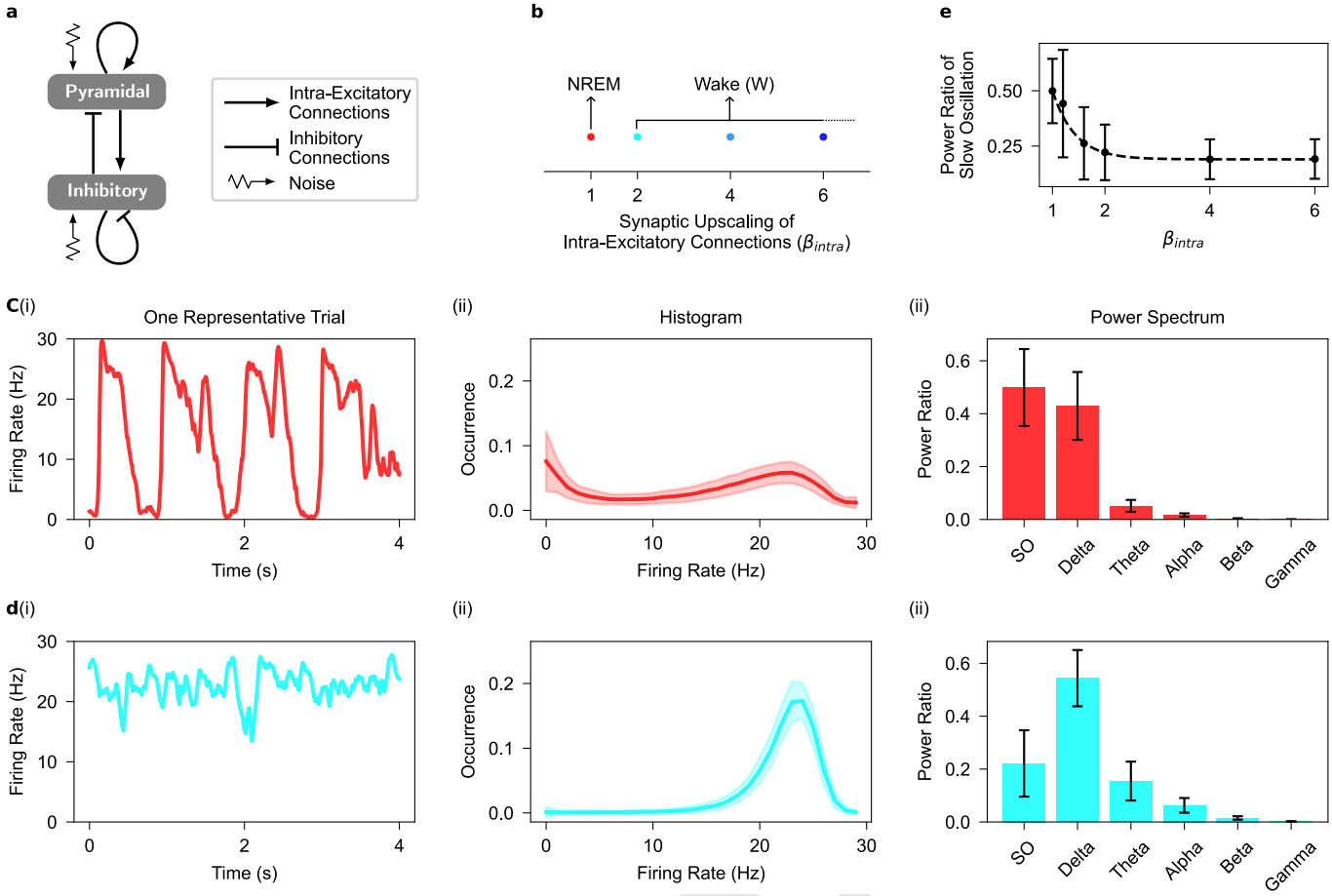

Fig. 1. Dynamical features of spontaneous firing activity in the one-cortical-column model. a, Diagram of the one-cortical-column model containing one pyramidal and one inhibitory population, where each population receives independent noise. The couplings between pyramidal and inhibitory populations are intra-excitatory and inhibitory connections mediated through, respectively, intra-AMPAergic and GABAergic synapses (Methods). Refer Table 1,2 for parameter description and values, respectively. **b**, Parameter space for synaptic upscaling of intra-excitatory connections (β_{intra}). **c**, Spontaneous firing rate signal for a representative trial (i), the distribution of firing rate signals (ii), and the power spectrum of signals (iii) when there is no intra-synaptic upscaling ($\beta_{intra} = 1$). The model produces electrophysiological features of NREM sleep when $\beta_{intra} = 1$. **d**, As in **c**, but for when intra-excitatory connections are upscaled ($\beta_{intra} = 2$). The model produces electrophysiological features of wakefulness when intra-excitatory connections are upscaled ($\beta_{intra} > 1$). **e**, The power ratio of slow oscillation (SO) gradually decreases with increasing intra-synaptic upscaling. Shaded area and Error bar correspond to standard deviation over 500 trials. SO, <1 Hz; Delta, 1-4 Hz; Theta, 4-7 Hz; Alpha, 7-13 Hz; Beta, 3-30 Hz; Gamma, 30-100 Hz.

ings in wakefulness. Nevertheless, the distribution of evoked response and spontaneous firing activities remain less separable during NREM sleep which compromises information detection in NREM sleep compared to synaptic upscalings in wakefulness (Extended Data Fig. 5).

Furthermore, our results indicate that it is distance-selective synaptic upscaling that enhances information differentiation in wakefulness compared to NREM sleep (Fig. 3c). These observations imply that synaptic upscaling during wakefulness does not enhance the encoded information content in the evoked responses unless it selectively favors inter- over intra-synaptic upscaling.

Two-cortical-column model. Next, we extended the model to two symmetric cortical columns. Given the symmetric connectivity paradigm in the two-cortical-column model, analysis of spontaneous firing activities were carried out on the pyramidal population in one of the cortical columns.

Electrophysiological patterns. Analysis of spontaneous firing activities in the two-cortical-column model (Fig. 4a) replicated the results obtained in the one-cortical-column model. In particular, intra-synaptic and inter-synaptic upscalings shifts the dynamics from NREM sleep towards wakefulness (Extended Data Fig. 6). However, it is important to note that the dynamical features of NREM sleep are compromised when connecting two cortical columns as compared to the one-cortical-column model (Extended Data Fig. 6a(i)-(iii) and Fig. 1c(i)-(iii)). These results are consistent with experimental observations indicating that cortical de-afferentation enhances the dynamical features of NREM sleep (13).

Evoked responses to inputs. In the context of the two-cortical-column model (Fig. 4a), one of the columns receives inputs directly, *perturbed cortical column*. The other cortical column, which does not receive direct inputs, is designated as the *unperturbed cortical column*. As in the one-cortical-column model, inputs are applied through inter-excitatory connections to the perturbed cortical column, ranging from 10 Hz to 90 Hz in increments of 20 Hz.

Noise-free evoked responses in the two-cortical-column model validate the findings observed in the one-cortical-

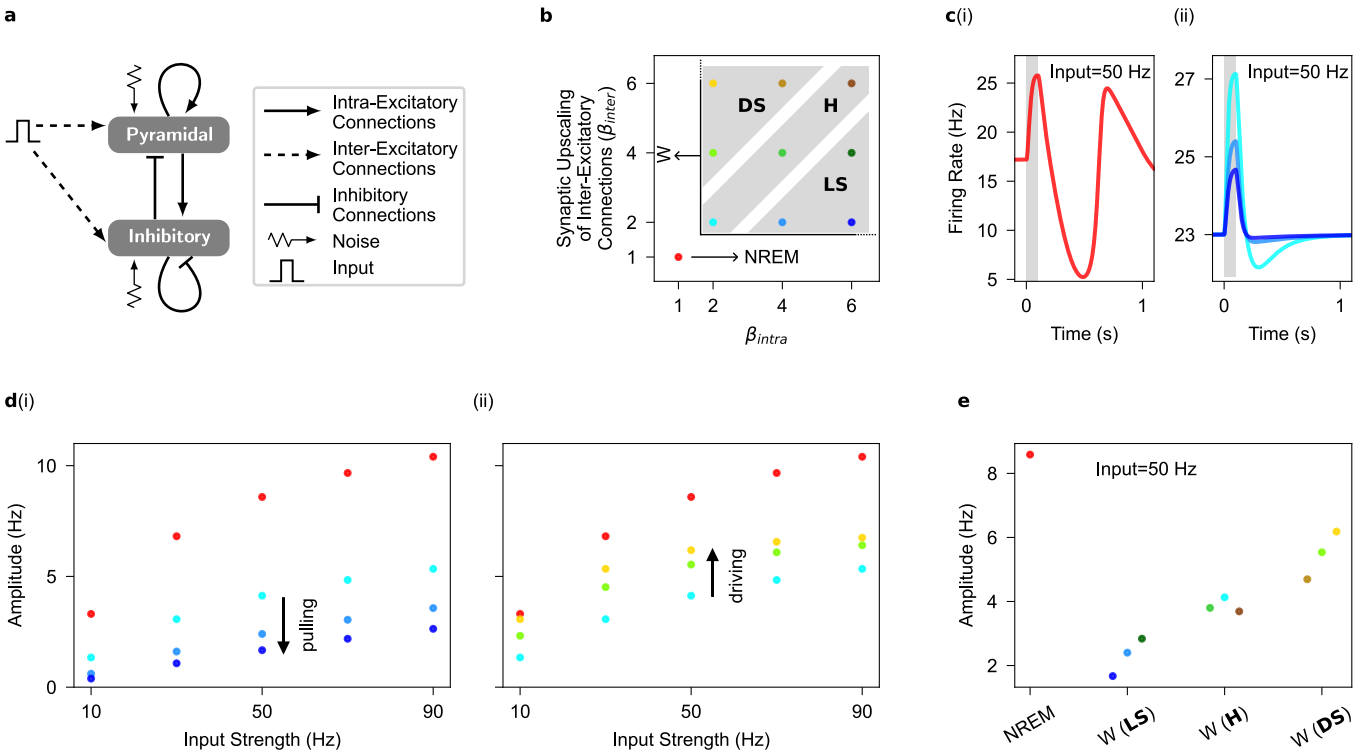

Fig. 2. Evoked firing responses to inputs in the one-cortical-column model. **a**, as in Fig. 1**a**, but for when the model is subjected to inputs. Inputs are applied through inter-excitatory connections mediated through inter-AMPAergic synapses. Note that the noise term is set to zero for noise-free evoked response. **b**, as in Fig. 1**a**, but for when intra- and inter-excitatory connections are upscaled in wakefulness. Note that synaptic upscaling in wakefulness can occur under three synaptic upscaling configurations: Local-Selective (LS: $\beta_{intra} > \beta_{inter} > 1$), Homogeneous (H: $\beta_{intra} = \beta_{inter} > 1$), and Distance-Selective (DS: $\beta_{inter} > \beta_{intra} > 1$). **c**, The evoked firing response in NREM sleep (i) and wakefulness (ii), when the input strength is 50 Hz, color coded as in Fig. 2**b** (the evoked firing responses for other synaptic upscalings in wakefulness are not shown here). **d**, Increasing intra-synaptic upscaling (from $\beta_{intra} = 2$ to $\beta_{intra} = 6$) while inter-synaptic upscaling is constant ($\beta_{inter} = 2$) during wakefulness produces a pulling effect on the amplitude of evoked firing responses (i). On the other hand, increasing inter-synaptic upscaling (from $\beta_{inter} = 2$ to $\beta_{inter} = 6$) while intra-synaptic upscaling is constant ($\beta_{intra} = 2$) during wakefulness produces a driving effect on the amplitude of evoked firing responses (ii). **e**, The amplitude of evoked firing responses increases as the synaptic upscaling transitions from local-selective (LS) to distance-selective (DS) upscaling during wakefulness.

Draft

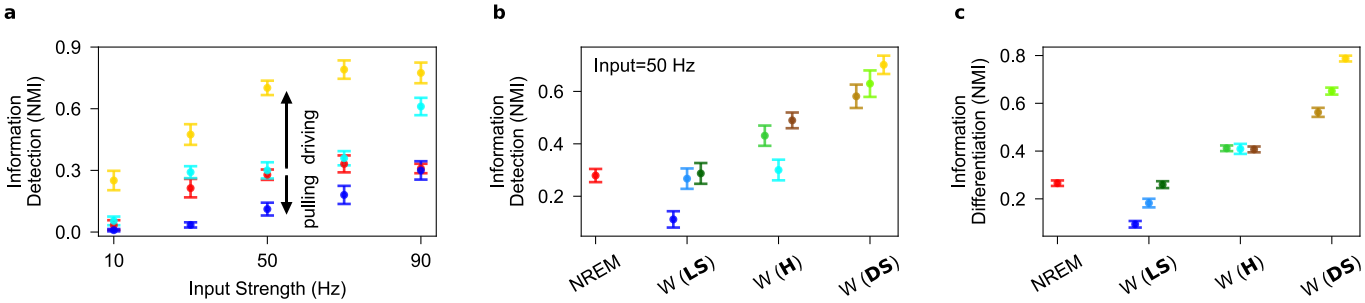

Fig. 3. Information content in the evoked firing responses to inputs in the one-cortical-column model. **a**, Increasing intra-synaptic upscaling while inter-synaptic upscaling is constant (from $\beta_{intra} = 2, \beta_{inter} = 2$ to $\beta_{intra} = 6, \beta_{inter} = 2$) during wakefulness produces a pulling effect on information detection. On the other hand, increasing inter-synaptic upscaling while intra-synaptic upscaling is constant (from $\beta_{intra} = 2, \beta_{inter} = 2$ to $\beta_{intra} = 2, \beta_{inter} = 6$) during wakefulness produces a driving effect on information detection. **b**, Information detection increases as the synaptic upscaling transitions from local-selective (LS) to distance-selective (DS) upscaling during wakefulness compared to NREM sleep. **c**, As in **b**, but for information differentiation. Information differentiation increases as the synaptic upscaling transitions from local-selective (LS) to distance-selective (DS) upscaling during wakefulness compared to NREM sleep. Error bar corresponds to 95% confidence interval over 10 performance estimate of the K-means clustering algorithms.

column model. Intra-synaptic upscaling produces a pulling effect on the amplitude of evoked responses in both the perturbed and unperturbed cortical columns (Fig. 4b(i),(ii)). On the other hand, inter-synaptic upscaling produces a driving effect on the amplitude of evoked responses (Fig. 4b(i),(ii)). Remarkably, the amplitude of evoked responses within both perturbed and unperturbed cortical columns increases as the synaptic upscaling transitions from local-selective to distance-selective upscaling (Fig. 4c(i),(ii) and Extended Data Fig. 7a(i),(ii)).

An intriguing observation is that intra- and inter-synaptic upscaling in the two-cortical-column model increase the spontaneous synaptic activity (Extended Data Fig. 7b(i),(ii)), indicating an intrinsic *pulling* effect associated with inter-excitatory connections. Nonetheless, inter-synaptic upscaling generates an overall driving effect as the net synaptic current ($\Delta E - \Delta I$, Methods) increases with increasing inter-synaptic upscaling, as opposed to intra-synaptic upscaling (Extended Data Fig. 7c(i),(ii)).

In the context of information content, information content in the perturbed cortical column increases as the synaptic upscaling transitions from local-selective to distance-selective upscaling in wakefulness compared to NREM sleep (Fig. 5a(i),(ii) and Extended Data Fig. 8a(i)-(iii)). Likewise, enhanced information content in the unperturbed cortical column is observed when inter-synaptic upscaling surpasses intra-synaptic upscaling (Fig. 5b(i),(ii) and Extended Data Fig. 8b(i)-(iii)). These findings underscore the hypothesis that a heterogeneous synaptic upscaling, favoring inter- over intra-synaptic upscaling, enhances the propagation of information content and neural responses in a hierarchal neural processing chain.

Robustness of the Computational Results. To quantify information content, we employed unsupervised machine learning techniques, such as K-means clustering algorithms. Notably, our results remain consistent even when supervised machine learning techniques, such as logistic classification algorithms (Methods), are applied (Extended Data Fig. 9a(i),(ii)).

Furthermore, our findings extend beyond machine learning techniques. The application of significance tests qualitatively reproduces the results pertaining to information detection and information differentiation (Methods and Extended Data Fig. 9b(i),(ii)). Moreover, information theory (Methods) was employed to compute the mutual information between the distribution of evoked responses at the input offset and the distribution of inputs. Interestingly, the mutual information increases as the synaptic upscaling transitions from local-selective to distance-selective upscaling during wakefulness (Extended Data Fig. 9c).

Discussion

Sleep and wakefulness exhibit distinctive behavioral, electrophysiological, and molecular characteristics (5), yet the causal connections between these biological layers remain elusive. This study delves into a specific relationship between two experimentally observed changes during the transition from sleep to wakefulness: synaptic upscaling of excitatory connections (18, 19) and enhanced cortical effective connectivity (2). Synaptic upscaling in wakefulness strengthens synaptic connections, a process compensated during sleep to maintain synaptic homeostasis. Enhanced cortical effective connectivity suggests a cortical gating mechanism, permitting external signals to reach higher processing cortical areas exclusively during wakefulness, potentially playing a role in the emergence of consciousness.

Our computational results establish a link between these phenomena, demonstrating that synaptic upscaling of excitatory connections not only induces dynamic changes in the electrical activity of the neural networks but also alters information propagation across these networks. However, we propose that for a spatially broader propagation of information and neural responses during wakefulness compared to NREM sleep, synaptic upscaling should preferentially occur between distinct networks rather than local and recurrent connections.

We acknowledge several limitations in our study. Firstly, our model is limited to interactions between two cortical columns and does not account for whole-brain interactions. A more complex connectivity model encompassing other cortical and subcortical structures could provide a comprehensive understanding of propagation of neural responses. Secondly, the connectivity between the two cortical columns is excitatory and symmetric, which may not fully represent the biological morphology across all cortical areas. Nevertheless, it is important to emphasize that our findings remain valid even when considering a single cortical column, as we have demonstrated that distance-selective synaptic upscaling enhances information encoding in response to inputs. Thirdly, our neural mass models operate on the assumption that neural communication relies on rate coding. Although our hypothesis is agnostic to the coding scheme, it would be beneficial for future research to explore spiking-based models to validate our results.

A notable strength of our study is the introduction of a novel synaptic mechanism that enhances the propagation of neural responses during wakefulness compared to NREM sleep. Our results align with several previously published studies. First, the strengthening of inter-areal excitatory connections in a balanced configuration has been shown to enhance signal transmission in a network model of the macaque cortex (33). Second, our hypothesis is consistent with the view that rare long-range connections are necessary for information processing (34).

The cerebral cortex and the thalamus innervate each other through massive direct excitatory projections (26). Therefore, the cortico-thalamo-cortical (CTC) pathways may play a pivotal role in enhancing the propagation of neural responses within the cerebral cortex during wakefulness. A recent study in mice, using Neuropixels probes during wakefulness and anesthesia, has suggested the necessity of burst firing mode in thalamic relay neurons for evoking cortical responses during wakefulness (35). However, it remains unclear why these patterns of evoked cortical responses would

DRAFT

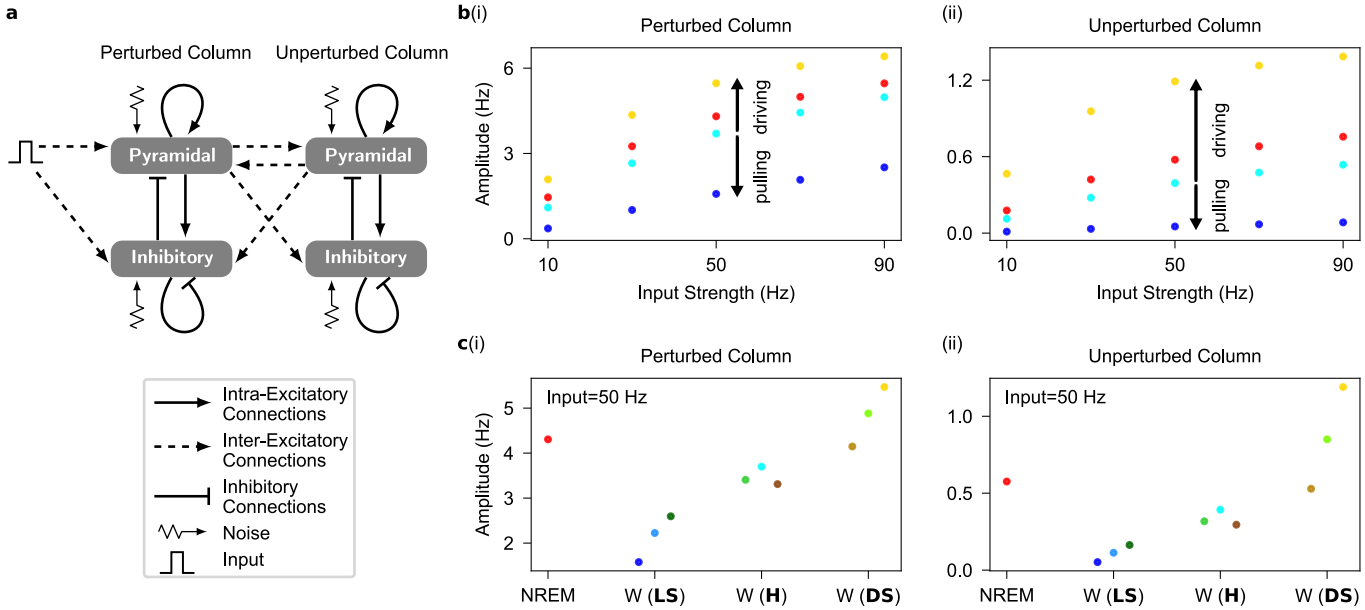

Fig. 4. Evoked firing responses to inputs in the two-cortical-column model. a, Diagram of the two-cortical-column model, where each population receives independent noise. The couplings between the two columns are symmetric and are inter-excitatory connections mediated through inter-AMPAergic synapses (refer Tables 1, 4, 5 for symbol description and parameter values). In the context of spontaneous firing activity, strength of the input is set to zero. Note that the noise term is set to zero for noise-free evoked response. **b**, Increasing intra-synaptic upscaling while inter-synaptic upscaling is constant (from $\beta_{intra} = 2, \beta_{inter} = 2$ to $\beta_{intra} = 6, \beta_{inter} = 2$) during wakefulness produces a pulling effect on the amplitude of evoked firing responses in the perturbed (i) and unperturbed cortical column (ii). On the other hand, increasing inter-synaptic upscaling while intra-synaptic upscaling is constant (from $\beta_{intra} = 2, \beta_{inter} = 2$ to $\beta_{intra} = 2, \beta_{inter} = 6$) during wakefulness produces a driving effect on the amplitude of evoked firing responses in the perturbed (i) and unperturbed cortical column (ii). **c**, The amplitude of evoked firing responses increases as the synaptic upscaling transitions from local-selective (LS) to distance-selective (DS) upscaling during wakefulness in the perturbed (i) and unperturbed cortical column (ii).

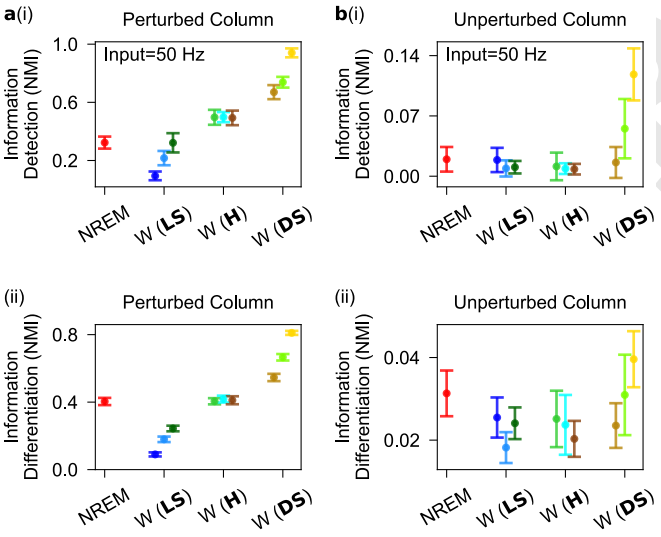

Fig. 5. Information content in the evoked firing responses to inputs in the two-cortical-column model. a, Information detection (i) and differentiation (ii) in the perturbed cortical column increase as the synaptic upscaling transitions from local-selective to distance-selective upscaling during wakefulness compared to NREM sleep. **b**, As in **a**, but for the unperturbed cortical column. Information detection (i) and differentiation (ii) in the unperturbed cortical column increase as the synaptic upscaling transitions from local-selective to distance-selective upscaling during wakefulness compared to NREM sleep. Error bar corresponds to 95% confidence interval over 10 performance estimate of the K-means clustering algorithms.

disappear in NREM sleep, given the higher propensity of thalamic neurons in NREM sleep for burst firing mode (36–38). Furthermore, experiments involving perturbations in cortical slices of ferrets, conducted in the absence of thalamic neurons, have shown that distinct response propagation patterns emerges in cortical slices under NREM- and wakefulness-like conditions (39). These observations suggest that changes in the dynamics of thalamic neurons and CTC synaptic pathways from NREM sleep to wakefulness do not solely serve as a comprehensive explanation.

Another mechanism influencing the flow of information among cortical areas may involve neural synchrony. Synchronous gamma activity has been suggested as a potential mechanism to account for varied response propagation during NREM sleep and wakefulness. However, experimental evidence indicates the inadequacy of changes in synchronous gamma activity as the sole explanatory mechanism (12, 13). Cortical areas can communicate not only through synchrony but also through coherence (40). According to the communication-through-coherence hypothesis, gamma-band (30-90 Hz) coherence can rapidly modulate excitation, evading subsequent inhibition and effectively activating postsynaptic neurons (41). Nevertheless, human studies have reported robust auditory-induced high-gamma (80-200 Hz) and low-gamma (40-80 Hz) power responses during both NREM sleep and wakefulness (4). Furthermore, it has been demonstrated that the inter-trial phase coherence in the 40 Hz range in response to 40-Hz click-trains in A1 and cortical areas outside A1 is preserved. This phenomenon suggests that the impairment of communication-through-coherence

may not offer a sufficient explanation for the attenuated response propagation during NREM sleep compared to wakefulness.

An intriguing possibility that may modulate the propagation of neural responses in the cerebral cortex is the shift in attention from NREM sleep to wakefulness. There is compelling experimental evidence that attention to external stimuli (42) and increased demands for higher sensory processing during wakefulness (43) enhance brain activation in response to external stimuli. Nonetheless, the enhanced propagation patterns in the cerebral cortex have been observed for Transcranial Magnetic Stimulation (2), which eliminates sensory perception of stimuli both during wakefulness and NREM sleep. Therefore, changes in attention cannot entirely account for the variations in response propagation across the sleep-wake cycle.

A unique aspect of our study is that we have introduced a framework for quantifying information content in neural signals. It is important to highlight that most studies in sleep research have not explicitly evaluated information content in evoked neural signals and are primarily based on the amplitude of evoked neural signals. In our study, we demonstrated that information encoding and propagation are not enhanced in wakefulness compared to NREM sleep unless inter-synaptic upscalings exceed intra-synaptic upscalings.

Our findings suggest that the synaptic homeostasis hypothesis should be applied heterogeneously at the circuit level. While our results require experimental validation, heterogeneity in synaptic upscalings has been observed at the cellular level for perforated and non-perforated synapses. Specifically, perforated synapses, on average, are larger and have a discontinuous postsynaptic density (PSD), while non-perforated synapses are smaller and have a continuous PSD (44). Studies have shown that in the cerebral cortex of mice, perforated synapses enlarge their axon-spine interface after waking relative to sleep, in contrast to the lack of change found in non-perforated synapses (44). This morphological change specific to perforated synapses supports their major role in synaptic plasticity and the selective implementation of synaptic homeostasis at the cellular level. Further experimental investigations are required to confirm whether heterogeneous synaptic homeostasis at the cellular level is related to the predictions made at the circuit level in our hypothesis.

In a broader context within the brain, heterogeneity appears to be a common rule rather than an exception. For instance, at the neural level, the firing phenotype of pyramidal neurons can differ based on their downstream projection areas, indicating heterogeneity within classical pyramidal cell types (45). At the synaptic level, synaptic integration onto pyramidal neurons occurs on separate dendritic structures (46) with different functional specializations (47). Furthermore, the developmental and regional expression of N-methyl-D-aspartate (NMDA) receptors has been reported to be heterogeneous (48). Our study suggests that enhanced cortical effective connectivity during wakefulness compared to NREM sleep might result from a heterogeneous rule in the brain: heterogeneous synaptic homeostasis.

Methods

The computational models implemented in this study have been previously described in earlier works (28, 29). In brief, we employed a neural mass model originally introduced by Wilson in 1972 (27) to replicate the average firing rate of a neural cortical column. This allowed us to capture the fundamental characteristics of both NREM sleep and wakefulness, as outlined in a prior research (28).

One-Cortical-Column Model. A single cortical column is composed of interconnected pyramidal (p) and inhibitory (i) populations (Fig. 1a).

Neural Mass Model. The average firing rate of each population is represented as an instantaneous function of the average membrane potential, denoted as $V_{p/i}$, using a sigmoid function (27, 49):

$$Q_k(V_k) = Q_k^{max} \frac{(1+\tanh(C(V_k-\theta_k)/\sigma_k))}{2}, \quad \textbf{(1)}$$

where $k \in \{p, i\}$. Q_k^{max}, θ_k, and σ_k correspond to, respectively, the maximum firing rate, firing rate threshold, and inverse neural gain of population p or i (refer Table 1,2 for symbol descriptions and parameter values). The constant C equals to $\frac{\pi}{2\sqrt{3}}$ and establishes the connection between the neural gain and the slope of the sigmoid function (28). This non-linear function aligns with experimental observations indicating that the firing rate and membrane potential of cortical neurons *in vivo* follow a non-linear increasing pattern (8).

Model Synapses. Connections between populations are modeled by dynamic synapses. Synapses within the model are characterized by presynaptic and postsynaptic elements. The presynaptic element consists of intrinsic and extrinsic activities. Intrinsic activity arises from explicitly modeled pyramidal and inhibitory populations, while extrinsic activity originates from nearby, non-explicitly modeled cortical columns. The extrinsic activity affects populations p and i exclusively through excitatory synapses. This is consistent with the morphology of cortical neurons, in which pyramidal neurons have larger projecting axons than the more localized inhibitory axons (20–22). This has also been reflected in numerous computational studies (50–54).

Our model follows Dale's principle, which dictates that excitatory populations exert excitatory effects on all synaptic connections, while inhibitory populations exert inhibitory effects, regardless of the identity of the target population. The postsynaptic component is characterized by ionotropic receptors, which include α-amino-3-hydroxy-5-methyl-4-isoxazolepropionic acid (AMPA) and γ-aminobutyric acid (GABA) receptors. To clarify, we consider synapses to be AMPAergic when they produce excitatory effects, which occurs when the presynaptic population is excitatory. Conversely, we categorize synapses as GABAergic when they generate inhibitory effects, and this happens when the presynaptic population is inhibitory. Henceforth, we will use the term *intra-excitatory connections* to refer to excitatory

DRAFT

Table 1. Parameter description in the one-cortical-column model.

Symbol	Description
$Q_k^{\max}$	Maximal firing rate of population k
θ_k	Firing rate threshold of population k (sigmoid function half activation)
σ_k	Inverse neural gain of the sigmoid function of population k
τ_k	Membrane time constant of population k
C_m	Membrane capacitance in the HH model
ϕ_k	Gaussian noise on population k
$N_{kk'}$	Mean number of synaptic connections from population k' to population k
γ_m	Time constant of the postsynaptic response of synapse type m
$\bar{g}_{\text{X}}$	Average X-ergic conductance
E_{X}	Reversal potential of the X-ergic current
$\bar{g}_{\text{KNa}}$	Average conductance of sodium-dependent potassium channel
E_{K}	Nernst reversal potential of potassium channel
τ_{Na}	Time constant of sodium extrusion
α_{Na}	sodium influx through population firing rate
R_{pump}	Strength of the sodium pump
Na_{eq}	Resting state sodium concentration equilibrium
β_{intra}	Synaptic-upscaling factor for intra-excitatory connections
β_{GABA}^k	Synaptic-upscaling factor for inhibitory connections on population k

Table 2. Parameter values in the one-cortical-column model.

Symbol	Value	Unit
$Q_p^{\max}$	30	Hz
$Q_i^{\max}$	60	Hz
θ_p, θ_i	-58.5	mV
σ_p	6.7	mV
σ_i	6	mV
τ_p, τ_i	30	ms
C_m	1	$\mu\text{F/cm}^2$
$\phi_{p/i}$	1.2	ms^{-1}
N_{pp}	144	–
N_{ip}	36	–
N_{pi}	160	–
N_{ii}	40	–
γ_p	$70 \cdot 10^{-3}$	ms^{-1}
γ_i	$58.6 \cdot 10^{-3}$	ms^{-1} -7 ,9
$\bar{g}_{\text{AMPA}}$	1	ms
$\bar{g}_{\text{GABA}}$	1	ms
E_{AMPA}	0	mV
E_{GABA}	-70	mV
E_{L}^p	-66	mV
E_{L}^i	-64	mV
$\bar{g}_{\text{KNa}}$	1.9	mS/cm^2
E_{K}	-100	mV
τ_{Na}	1.7	ms
α_{Na}	2	$\text{mM} \cdot \text{ms}$
R_{pump}	0.09	mM
Na_{eq}	9.5	mM
β_{intra}	1	–
$\beta_{\text{GABA}}^{p/i}$	1	–

connections within a cortical column, which are mediated through intra-AMPAergic synapses.

The mathematical framework utilized to describe synapses involves convolving the presynaptic firing rate, $Q_{k'}$, with the average synaptic response to a single spike, $\alpha_{k'}$, which exhibits an exponential decay time course (55):

$$s_{kk'} = N_{kk'} Q_{k'}(V_{k'}) \circledast \alpha_{k'}, \quad \textbf{(2)}$$

$$\alpha_{k'} = \gamma_{k'}^2 \, t \, \exp(-\gamma_{k'} t), \quad \textbf{(3)}$$

where $N_{kk'}$ represents the average number of synaptic connections from the presynaptic population k' to the postsynaptic population k. The parameter $\gamma_{k'}$ characterizes the time constant governing the dynamics of a synapse activated by the presynaptic firing of population k'. The combination of equations (2) and (3) leads to a second-order differential equation:

$$\ddot{s}_{kk'} = \gamma_{k'}^2 \left(N_{kk'} \, Q_{k'}(V_{k'}) + \phi_k - s_{kk'} \right) - 2\gamma_{k'} \, \dot{s}_{kk'}, \quad \textbf{(4)}$$

Equation (4) describes the synaptic current dynamics resulting from the firing of the presynaptic population k' on the postsynaptic population k. Additionally, noise, denoted as ϕ_k, is independently simulated for each cortical population as a Gaussian process with zero autocorrelation time, zero mean, and a standard deviation of 1.2 ms^{-1}. Notably, the application of Gaussian noise is limited to intra-excitatory connections. The intra-AMPAergic and GABAergic synaptic currents are defined as follows:

$$I_{intra\text{-AMPA}}^k = \beta_{intra} \, \bar{g}_{\text{AMPA}} \, s_{kp} \, (V_k - E_{\text{AMPA}}), \quad \textbf{(5)}$$

$$I_{\text{GABA}}^k = \beta_{\text{GABA}}^k \, \bar{g}_{\text{GABA}} \, s_{ki} \, (V_k - E_{\text{GABA}}), \quad \textbf{(6)}$$

DRAFT

here, β_{intra} and β^k_{GABA} are scaling factors for intra-excitatory connections and inhibitory connections on population k, respectively. $\bar{g}_{\text{AMPA}}$ and $\bar{g}_{\text{GABA}}$ correspond to the average AMPAergic and GABAergic conductances, while E_{AMPA} and E_{GABA} represent the reversal potentials for AMPAergic and GABAergic currents, respectively.

The dynamics of the average membrane potential for each cortical population ($V_{p/i}$) are determined using the mathematical formalism of the classical conductance-based model (56). This model encompasses one leak, two synaptic currents, and an activity-dependent potassium current, as described by the following equations:

$$\tau_p \dot{V}_p = -I^p_{\text{L}} - I^p_{intra\text{-AMPA}} - I^p_{\text{GABA}} - \tau_p C_m^{-1} I_{\text{KNa}}, \quad \textbf{(7)}$$

$$\tau_i \dot{V}_i = -I^i_{\text{L}} - I^i_{intra\text{-AMPA}} - I^i_{\text{GABA}}, \quad \textbf{(8)}$$

Here, $\tau_{p/i}$, $I^{p/i}_{\text{L}}$, $I^{p/i}_{intra\text{-AMPA}}$, and $I^{p/i}_{\text{GABA}}$ represent, respectively, the membrane time constant, leak, intra-AMPAergic, and GABAergic currents of population p or i. The variable I_{KNa} denotes the activity-dependent potassium current specific to the pyramidal population, which is detailed in the following subsection. Additionally, C_m signifies the membrane capacitance in the Hodgkin–Huxley model.

Activity-Dependent Potassium Current. The slow oscillation is a prominent feature of neuronal cortical activity during NREM sleep, characterized by alternating active (Up) and silent (Down) firing patterns. The initiation of the Down state has been hypothesized to involve the activation of the slow activity-dependent K^+ current, as suggested in previous studies (30–32). The sodium-dependent potassium current I_{KNa} and sodium concentration [Na] are incorporated into the model as follows:

$$I_{\text{KNa}} = \bar{g}_{\text{KNa}} \frac{0.37}{1 + (\frac{38.7}{[\text{Na}]})^{3.5}} (V_p - E_{\text{K}}), \quad \textbf{(9)}$$

$$\tau_{\text{Na}} [\dot{\text{Na}}] = \alpha_{\text{Na}} Q_p(V_p) - \text{Na}_{\text{pump}}([\text{Na}]), \quad \textbf{(10)}$$

In these equations, $\bar{g}_{\text{KNa}}$, E_{K}, τ_{Na}, and α_{Na} represent the average conductance of I_{KNa}, the Nernst reversal potential of the I_{KNa} current, the time constant governing the extrusion of sodium concentration, and the average influx of sodium concentration per firing event, respectively. The function Na_{pump} accounts for sodium pumps that regulate the removal of sodium ions.

Synaptic Upscaling of Intra-Excitatory Connections. The average conductance of intra-excitatory connections within the one-cortical-column model are upscaled by a factor of β_{intra}. Primarily, we demonstrate that the one-cortical-column model generates NREM-like dynamics when there is no synaptic upscaling, i.e., $\beta_{intra} = 1$. Next, we show that intra-synaptic upscaling induces a transition in the dynamics from NREM sleep to wakefulness, in line with the concept of synaptic homeostasis hypothesis (18, 19) and the influence of active neuromodulatory inputs on synaptic upscaling from subcortical regions (5, 6).

In the one-cortical-column model, synaptic upscaling of intra-excitatory connections within the cortical column is achieved by increasing the parameter β_{intra}. The intra-synaptic upscaling process is carried out in a balanced configuration. To elaborate, it involves enhancing inhibition to counteract overexcitation within each population. Consequently, the average conductance of inhibitory connections is augmented in both pyramidal and inhibitory populations. This augmentation is governed by the factors β^p_{GABA} and β^i_{GABA}, respectively (refer Table 3 for parameter values).

Table 3. Parameter values of β^k_{GABA} for intra-synaptic upscalings in wakefulness in the one-cortical-column model.

	$\beta_{intra} = 2$	$\beta_{intra} = 3$	$\beta_{intra} = 4$
β^p_{GABA}	1.961	4.724	7.488
β^i_{GABA}	2.165	4.65	7.134

This approach ensures that the intra-synaptic upscalings remain in balance by maintaining the steady-state values of the average membrane potential for both pyramidal (V_p) and inhibitory (V_i) populations, aligning them with their respective values during the Up state in NREM sleep. This is in agreement with experimental findings that reported dynamics of neural signals in Up states during NREM sleep are similar to those of continuous wakefulness (8, 57).

The values of V_p and V_i during Up state in NREM sleep (when there is no synaptic upscaling: $\beta_{intra} = 1$) are determined through 500 simulations, each lasting 4 seconds. During NREM sleep, the distribution of firing rate signals exhibits a bimodal pattern, with the polarized peak being associated with the Up states. The peak value of the distribution of firing rate signals during Up states is employed to calculate the steady-state values of V_p and V_i in wakefulness. The parameters β^p_{GABA} and β^i_{GABA}, pertaining to pyramidal and inhibitory populations, respectively, are adjusted to align V_p and V_i with their counterparts during the Up state for a given intra-synaptic upscaling parameter, β_{intra}, in wakefulness. For the complete model equations, please refer to Appendix . Further details regarding the dynamical constraints governing β^p_{GABA} and β^i_{GABA} for pyramidal and inhibitory populations in the one-cortical-column model are available in Appendix .

Two-Cortical-Column Model. We have expanded the model to encompass two bidirectionally connected cortical columns (Fig. 4a). The parameters for each individual cortical column remain consistent with those described in the one-cortical-column model. Our assumption is that the connectivity between these two cortical columns is both symmetrical and excitatory. This is attributed to the longer axons of pyramidal neurons compared to the shorter axons of inhibitory neurons, as substantiated by previous studies (20–22, 50–52, 54). For the sake of notation convenience, we will utilize p and i to denote the pyramidal and inhibitory populations in the first cortical column, and p' and i' to denote populations in the second cortical column (refer to Table 4

DRAFT

for the specific values of connectivity between the two cortical columns).

Table 4. Parameter values of connectivity in the two-cortical-column model.

Symbol	Value	Description
$N_{pp'}$, $N_{p'p}$	16	Mean number of synaptic connections from p to p' (and p' to p)
$N_{ip'}$, $N_{i'p}$	4	Mean number of synaptic connections from p to i' (and p' to i)

In the context of the two-cortical-column model, we will refer to excitatory synapses connecting the two columns as *inter-excitatory connections*, distinguishing them from the *intra-excitatory connections* within each individual cortical column.

In accordance with the description provided, the second-order differential equations for inter-AMPAergic postsynaptic responses in the first cortical column due to the inter-excitatory connections coupling are expressed as follows:

$$\ddot{s}_{pp'} = \gamma_{p'}^2 \left(N_{pp'}\, Q_{p'}(V_{p'}) - s_{pp'}\right) - 2\gamma_{p'}\, \dot{s}_{pp'}, \quad \textbf{(11)}$$

$$\ddot{s}_{ip'} = \gamma_{p'}^2 \left(N_{ip'}\, Q_{p'}(V_{p'}) - s_{ip'}\right) - 2\gamma_{p'}\, \dot{s}_{ip'}, \quad \textbf{(12)}$$

Here, $N_{kp'}$ represents the mean number of synaptic connections from a presynaptic pyramidal population p' in the second cortical column to postsynaptic populations k, $k \in \{p,\, i\}$, in the first cortical column. Consequently, the inter-AMPAergic current to the postsynaptic population k in the first cortical column can be defined as:

$$I^k_{inter\text{-AMPA}} = \beta_{inter}\, \bar{g}_{\text{AMPA}}\, s_{kp'}\, (V_k - E_{\text{AMPA}}), \quad \textbf{(13)}$$

Consequently, the dynamics of the average membrane potential of each cortical population, $V_{p/i}$, are determined as follows:

$$\tau_p \dot{V}_p = -I^p_{\text{L}} - I^p_{intra\text{-AMPA}} - I^p_{inter\text{-AMPA}} - I^p_{\text{GABA}} - \tau_p C_m^{-1} I_{\text{KNa}}, \quad \textbf{(14)}$$

$$\tau_i \dot{V}_i = -I^i_{\text{L}} - I^i_{intra\text{-AMPA}} - I^p_{inter\text{-AMPA}} - I^i_{\text{GABA}}, \quad \textbf{(15)}$$

Swapping indexes between the first and second cortical column results in the equations for the second cortical column. see Appendix for the full model equations.

During NREM sleep, these inter-excitatory connections increase excitation in both the pyramidal and inhibitory populations within each cortical column. To counterbalance this overexcitation, the average conductance of inhibitory connections within each cortical column is upregulated by a factor denoted as β^k_{GABA}, $k \in \{p,\, i,\, p',\, i'\}$. This adjustment is achieved by first determining the steady-state values of V_p and V_i in the one-cortical-column model through a noise-free simulation (in the absent of Gaussian noise) during NREM sleep. These values are then used to compute the corresponding β^k_{GABA}, $k \in \{p,\, i,\, p',\, i'\}$, in the two-cortical-column model during NREM sleep (for further details, please refer to Appendix for the dynamical constraints on β^k_{GABA} in the two-cortical-column model). It is important to note that due to the symmetry in the connectivity paradigm, the values for the pyramidal populations in each cortical column are identical, as are the values for the inhibitory populations (refer Table 5 for the parameter values of β^k_{GABA} during NREM when $\beta_{intra} = 1$ and $\beta_{inter} = 1$).

During wakefulness in the two-cortical-column model, synaptic upscaling occurs in two directions: intra-excitatory connections and inter-excitatory connections. As a result, there are three synaptic upscaling configurations in wakefulness: local-selective ($\beta_{intra} > \beta_{inter} > 1$), homogeneous ($\beta_{intra} = \beta_{inter} > 1$), and distance-selective synaptic upscaling ($\beta_{inter} > \beta_{intra} > 1$). In each of these cases, synaptic upscaling introduces overexcitation within each cortical column. To counteract this overexcitation, the average conductance of inhibitory connections within each cortical column is upregulated by β^k_{GABA}, with k representing $p,\, i,\, p',\, i'$. This adjustment is made by utilizing the values of V_p and V_i in Up states from the one-cortical-column model. Subsequently, β^k_{GABA}, with k being $p,\, i,\, p',\, i'$, is upregulated until the corresponding V_p and V_i values are achieved for the intra- and inter-synaptic upscaling in wakefulness, denoted as β_{intra} and β_{inter}, respectively (for further details, please refer to Appendix for the dynamical constraints on β^k_{GABA} in the two-cortical-column model). This ensures that the steady-state values of V_p and V_i in the two-cortical-column model align with the values in wakefulness and Up states of NREM sleep in the one-cortical-column model (refer Table 5 for the parameter values of β^k_{GABA} during NREM sleep when $\beta_{intra} = \beta_{inter} = 1$ and during wakefulness when $\beta_{intra} > 1, \beta_{inter} > 1$).

Computational pipeline. Simulations were implemented in Python and conducted using a stochastic Heun method (58) with a step size of 0.1 ms. The code is available on GitHub. Each simulation (trial) was implemented independently, with initial conditions for all variables randomly selected from a uniform distribution. Trials were simulated with a duration of 4 s, after discarding the first 4 s at the beginning of the simulation to eliminate transient dynamics and stabilize the solution.

The computational pipeline consisted of two stages. In the first stage, we simulated signals for the one-cortical-column model, and in the second stage, we extended this to the two-cortical-column model. Each stage comprised two phases. The first phase focused on simulating stochastic signals in the absence of external inputs to asses the *electrophysiological patterns* (subsection and) of the spontaneous neural activities in the respective model. Initially, 500 trials were simulated separately when excitatory synapses were not upscaled (refer Table 2). This showed that the model was capable of producing NREM-like dynamics. Moreover, in the one-cortical-column model, 500 independent trials were simulated separately to evaluate the robustness of NREM-like dynamics as the standard deviation of the Gaussian noise was varied by 10%. This analysis demonstrated that the NREM-

DRAFT

Table 5. Parameter values of β^k_{GABA}, $k \in \{p,\ i,\ p',\ i'\}$, for various synaptic upscalings in the two-cortical-column model.

	$\beta_{intra} = 1$	$\beta_{intra} = 2$			$\beta_{intra} = 4$			$\beta_{intra} = 6$		
	$\beta_{inter} = 1$	$\beta_{inter} = 2$	$\beta_{inter} = 4$	$\beta_{inter} = 6$	$\beta_{inter} = 2$	$\beta_{inter} = 4$	$\beta_{inter} = 6$	$\beta_{inter} = 2$	$\beta_{inter} = 4$	$\beta_{inter} = 6$
$\beta^{p/p'}_{\text{GABA}}$	1.18	2.268	2.575	2.882	5.032	5.339	5.646	7.795	8.102	8.409
$\beta^{i/i'}_{\text{GABA}}$	1.149	2.441	2.717	2.993	4.926	5.202	5.478	7.41	7.686	7.963

like dynamics remained consistent within the examined range and was independent of the standard deviation of the Gaussian noise. Finally, 500 trials were conducted separately to explore the impact of various synaptic upscalings in a balanced configuration in the respective model. These trials revealed how synaptic upscaling could shift the dynamics from NREM-like to wakefulness-like dynamics.

In the second phase we focused on simulating signals when the respective model is subjected to inputs with increasing input strength to asses the *evoked responses to inputs* (subsection and). Inputs are delivered through inter-excitatory connections and represent the strength of presynaptic firing of an unmodeled pyramidal population, denoted as $Q^{\text{input}}_{p^{um}}$. We consider that the unmodeled upstream cortical column forms excitatory synapses with the pyramidal and inhibitory populations in the one-cortical-column model. The mean number of synaptic connections is specified as $N_{pp^{um}}$ and $N_{ip^{um}}$ (16 and 4, respectively). The index "um" denotes the unmodeled cortical column. The inter-AMPAergic postsynaptic response in the cortical column resulting from the firing of the unmodeled upstream cortical column is described by the equation:

$$\ddot{s}^{\text{input}}_{kp^{um}} = \gamma^2_{p^{um}}\ (N_{kp^{um}}\ Q^{\text{input}}_{p^{um}} - s^{\text{input}}_{kp^{um}}) \\ -2\gamma_{p^{um}}\ \dot{s}^{\text{input}}_{kp^{um}}, \tag{16}$$

Here, k represents either the pyramidal or the inhibitory postsynaptic population in the cortical column model. Considering the influence of inter-excitatory connections from the unmodeled cortical column, the excitatory postsynaptic current to the postsynaptic population k in response to a given input strength can be expressed as follows:

$$I^{k,\ \text{input}}_{inter\text{-AMPA}} = \beta_{inter}\ \bar{g}_{\text{AMPA}}\ s^{\text{input}}_{kp^{um}}\ (V_k - E_{\text{AMPA}}) \tag{17}$$

for $k \in \{p, i\}$. Taking in to account these postsynaptic currents associated with the input, the equations for the dynamics of the average membrane potential of each cortical population in the one-cortical-column model, as given by equation 7 and 8, can be expressed as follows:

$$\tau_p \dot{V}_p = -I^p_{\text{L}} - I^p_{intra\text{-AMPA}} - I^p_{\text{GABA}} - \tau_p C_m^{-1} I_{\text{KNa}} \\ - I^{p,\ \text{input}}_{inter\text{-AMPA}}, \tag{18}$$

$$\tau_i \dot{V}_i = -I^i_{\text{L}} - I^i_{intra\text{-AMPA}} - I^i_{\text{GABA}} - I^{i,\ \text{input}}_{inter\text{-AMPA}}, \tag{19}$$

In the context of the two-cortical-column model, the equations for the dynamics of the average membrane potential of each cortical population, $V_{p/i}$, as described by equation 14 and 15, can be expressed as follows:

$$\tau_p \dot{V}_p = -I^p_{\text{L}} - I^p_{intra\text{-AMPA}} - I^p_{inter\text{-AMPA}} - I^p_{\text{GABA}} \\ - \tau_p C_m^{-1} I_{\text{KNa}} - I^{p,\ \text{input}}_{inter\text{-AMPA}}, \tag{20}$$

$$\tau_i \dot{V}_i = -I^i_{\text{L}} - I^i_{intra\text{-AMPA}} - I^p_{inter\text{-AMPA}} - I^i_{\text{GABA}} \\ - I^{i,\ \text{input}}_{inter\text{-AMPA}}, \tag{21}$$

DRAFT

Inputs are depicted as boxcar functions, each lasting 100 milliseconds. Specifically, the variable $Q_{p^{um}}^{\text{input}}$ maintains a value of zero both before the input onset and after the input offset. In the context of the two-cortical-column model, one of the columns receives the inputs directly, hereafter referred to as the *perturbed cortical column*. The other cortical column, which does not receive direct inputs, is designated as the *unperturbed cortical column*. It is important to note that $Q_{p^{um}}^{\text{input}}$ remains at zero for the unperturbed cortical column, so does $I_{inter\text{-AMPA}}^{k,\ \text{input}}$, where k can represent either p' or i'.

Initially, we carry out a single noise-free trial in which the respective model is subjected to inputs with increasing input strength. This trial is designed to evaluate noise-free evoked responses for NREM sleep and various synaptic upscalings in wakefulness. Subsequently, we conduct 500 independent trials separately for NREM sleep and various synaptic upscalings in wakefulness within the corresponding model. These trials are intended to assess stochastic evoked responses.

Data Analysis

All data analyses were conducted offline using Python. Our analysis primarily focused on the firing rate signals generated by the pyramidal populations.

Analysis of Electrophysiological Patterns. In the first phase of each stage in the computational pipeline, we assessed the dynamic characteristics of spontaneous activities. This involved 500 independent trials for NREM sleep and synaptic upscalings in wakefulness (Fig. 1c(i)). Due to the symmetric connectivity paradigm in the two-cortical-column model, the analysis of spontaneous activities was confined to the pyramidal population in one of the cortical columns.

Analysis of amplitude-frequency content of firing rate signals. To assess the variability in the amplitude of spontaneous firing rate activities, we calculated the normalized distribution of firing rate signals for each brain state (NREM and various synaptic upscalings in wakefulness) separately, using a bin size of 1 mV (Fig. 1c(ii)).

To examine the variability in the frequency content of spontaneous firing rate activities, we generated spectrograms of firing rate signals for each brain state. This process involved segmenting each firing rate signal into 2-second intervals with a 90% overlap, assuming quasi-stationarity within each window (59). Each window was tapered using a Hann function to mitigate spectral leakage. We computed the Short-Time Fourier Transform (STFT) and derived the power spectral density (PSD) for each time window. Since the brain states were independently simulated and not time-locked events, we averaged the PSD over all time windows separately for each brain state (60). To visualize the wide dynamic range of firing rate signals, we represented the spectrogram in logarithmic decibels (dB) using the formula:

$$\text{dB} = \log_{10}\left(\frac{P}{P_r}\right), \tag{22}$$

where P represents the averaged PSD, and P_r denotes the reference PSD, which is set at 1 $(\text{mV})^2/\text{Hz}$. The spectrogram of firing rate signals was averaged over 500 trials for each brain state. To quantify changes in each frequency band, we calculated the power ratio of each frequency band relative to the total power within each signal (Fig. 1c(iii)). This ratio was averaged over 500 trials.

Analysis of Evoked Responses to Inputs.

Analysis of noise-free evoked responses. Noise-free evoked responses were assessed for both one- and two-cortical-column models subjected to inputs with increasing strength. The amplitude of evoked firing responses was extracted at the input offset subtracting the prestimulus values. These noise-free evoked responses provided insights into the influence of intra- and inter-synaptic upscaling on the amplitude of evoked responses, showcasing the *pulling* and *driving* effects, respectively (Fig. 2d(i),(ii)). This analysis was performed for NREM sleep and various synaptic upscaling configurations in wakefulness.

We also computed the synaptic excitation (E) and synaptic inhibition (I) on pyramidal populations for NREM sleep and various synaptic upscalings in wakefulness in both one- and two-cortical-column models. The E and I are defined as follows:

$$\text{E} = |I_{intra\text{-AMPA}}^{k} + I_{inter\text{-AMPA}}^{k} + I_{inter\text{-AMPA}}^{k,\ \text{input}}|, \tag{23}$$

$$\text{I} = |I_{\text{GABA}}^{k}|, \tag{24}$$

$$\tag{25}$$

where k is p in the one-cortical-column model and $k \in \{p,\, p'\}$ in the two-cortical-column model. Note that $I_{inter\text{-AMPA}}^{k}$ is zero in the one-cortical-column model and $I_{inter\text{-AMPA}}^{k,\ \text{input}}$ is zero for the unperturbed cortical column in the two-cortical-column model.

The E and I values were extracted from the noise-free simulations of the corresponding models. This approach was chosen because the average of this ratio computed in the stochastic condition will converge to the noise-free value for a sufficiently large number of trials. Spontaneous synaptic activity was defined as E+I (Extended Data Fig. 3a). The evoked E (ΔE) and the evoked I (ΔI) values were also computed by subtracting the values of E and I at the input offset from the corresponding peristimulus values. The net evoked synaptic current was defined as $\Delta\text{E}-\Delta\text{I}$ (Extended Data Fig. 3b).

Analysis of stochastic evoked responses. Stochastic evoked responses were assessed for both the one- and two-cortical-column models under various input strengths. We conducted 500 independent trials for each input strength separately in the context of NREM sleep and all synaptic upscalings in wakefulness.

To evaluate the stochastic evoked firing responses, we developed a comprehensive framework for quantifying the information content in neural signals. This framework leverages

DRAFT

various techniques, including machine learning methods, significance tests, and information theory, to estimate the information content within the stochastic evoked responses. We applied this framework to assess the information content in the evoked firing responses at the input offset.

Information Quantification. Neural firing can originate either spontaneously or as a response to an external stimulus. In a simplified model of hierarchical neural processing, a group of neurons (or a single neuron) responds to external stimuli by generating neural firing responses. These responses, in turn, influence the firing activity of postsynaptically connected neurons (or a single neuron), and so forth (61, 62). The neural spikes in the postsynaptic group contain information about the neural firing responses of the presynaptic group, which, in turn, holds information about the external stimuli. We define information from the perspective of a neuron as *"a difference that makes a difference"* (63). To quantify information in neural firing responses, we propose two measures: *information detection* and *information differentiation*.

Information detection. Information detection determines whether neural firing responses to a stimulus significantly differ from spontaneous neural firing. In essence, it assesses whether neural firing responses can be statistically attributed to the presentation of a stimulus. However, while information detection is essential for perception, it doesn't guarantee a high level of information about external stimuli encoded in neural firing responses. For example, if neural firing responses to two different stimuli each significantly differ from spontaneous neural firing activities but not significantly from each other, it indicates a lack of information to distinguish between stimuli. This does not imply a lack of information content but rather attenuated information content, as it can still distinguish neural firing responses from spontaneous activities.

Information differentiation. Information differentiation determines whether neural firing responses to different stimuli significantly differ from each other. It assesses whether neural firing responses can be statistically attributed to distinct stimuli. This measure is limited to the set of stimuli being tested. Information differentiation in neural firing responses can be high for a specific set of stimuli but may decrease with the introduction of new stimuli.

Information detection and differentiation together determine information content in neural firing responses. High levels of information detection and differentiation ensure accurate decoding of stimuli features from neural firing responses by an ideal observer with prior knowledge about the stimuli. Note that this framework for quantifying information content holds true for both spike-based and rate-based theories and whether neural coding is signal correlation or noise correlation.

Information propagation. Changes in information propagation between two neural groups in a hierarchical processing chain under different conditions can be quantified by measuring information content in each group. For instance, let's assume that information content in a presynaptic neural group is preserved in two different brain states. If information detection is preserved while differentiation is not in the postsynaptic neural group from one brain state to the other, it suggests that information content in the postsynaptic group is attenuated in the transition from one brain state to the other. It implies a reduced flow of information from the presynaptic to the postsynaptic group when the brain state switches. Changes in information detection and differentiation are not mutually exclusive; both can decrease in one brain state compared to another.

To quantify information detection and differentiation in a neural group, unsupervised and supervised machine learning algorithms can be utilized. Information detection is determined by how well a specific machine learning algorithm distinguishes between neural firing responses to a stimulus in poststimulus intervals and spontaneous neural firing activities in peristimulus intervals. Likewise, information differentiation is determined by how well a specific machine learning algorithm distinguishes among neural firing responses in poststimulus intervals to different stimuli.

Machine Learning Techniques.

Unsupervised framework. In the unsupervised framework, we employed the K-means clustering method to quantify information content in neural signals. The K-means clustering algorithm proceeded with three steps: identifying the number of clusters, estimating cluster centroids, and predictions.

To measure information detection, a K-means clustering method was derived separately for each input strength in NREM sleep and all synaptic upscalings in wakefulness to cluster the data, x. x represents the firing rate of the pyramidal population and consisted of 2×500 values (500 values for spontaneous firing activities and 500 values for evoked firing responses to a given input strength). We determined the number of clusters as two (for spontaneous and evoked clusters) and initialized corresponding cluster centroids randomly. Data were divided into training and test sets. The algorithm iteratively updated the cluster centroids using the training data and converged when centroids were stabilized. The trained cluster centroids were then used to predict the cluster label of data points in the test set (assigning each data point to the nearest cluster).

The performance of the clustering algorithm in predicting cluster labels was evaluated using Normalized Mutual Information (NMI) as an external validation technique, given access to the true labels (64). NMI measures the similarity between the predicted cluster labels, $C = \{C_1, C_2, \ldots, C_K\}$, and the true labels, $C' = \{C'_1, C'_2, \ldots, C'_{K'}\}$. Note that K and K' are equal to the number of clusters ($K = K' = 2$ for information detection). First, the mutual information between the predicted cluster labels and the true labels, $\mathrm{MI}(C, C')$, was computed as:

$$\mathrm{MI}(C, C') = \sum_{k=1}^{K} \sum_{k'=1}^{K'} p(k, k') \log_2 \frac{p(k, k')}{p(k)p(k')}, \qquad \textbf{(26)}$$

where $p(k)$ and $p(k')$ are, respectively, the probability of a

DRAFT

given data point belonging to C_k in clustering C and to $C'_{k'}$ in clustering C'. $p(k,k')$ is the joint probability of the given data point that belongs to C_k and $C'_{k'}$. $\mathrm{MI}(C,C')$ determines how much uncertainty is reduced about the true labels of data, C', by knowing predicted cluster labels, C, in the K-means clustering algorithm (65). Next, it is normalized to range between 0 and 1, indicating, respectively, no agreement and perfect agreement between the predicted and the true labels (64):

$$\mathrm{NMI}(C,C') = \frac{\mathrm{MI}(C,C')}{\sqrt{H(C)H(C')}}, \quad \textbf{(27)}$$

$$H(C) = -\sum_{k=1}^{K} p(k)\log_2 p(k), \quad \textbf{(28)}$$

where $H(C)$ and $H(C')$ are, respectively, the entropy associated with clustering C and C'. Higher NMI values indicate greater information detection.

To assess the effectiveness of the algorithm, we performed 10-fold cross-validation (66) and used stratified random sampling to eliminate the effect of data imbalances in training and test sets. Briefly, data were partitioned randomly into 10 subsets (folds) of equal size. Samples in all subsets except the first subset were used as the training set to estimate the cluster centroids. The held-out subset was used as the test set to estimate algorithm performance. The procedure repeated for all other subsets such that all subsets were used only once as the test set. The performance of the algorithm is then reported as the average over 10 performance estimates from the 10-fold cross-validation along with the 95% confidence interval (Fig. 3a).

To measure information differentiation, a K-means clustering method was derived separately in NREM sleep and all synaptic upscalings in wakefulness to cluster the data, x. x represents the firing rate of the pyramidal population and consisted of $N \times 500$ values, where N is the number of inputs (500 values for evoked firing responses to each input strength). We determined the number of clusters as the number of inputs, N. As in information detection, we used stratified 10-fold cross-validation to estimate cluster centroids and the performance of the algorithm. The NMI (see equation 27) was computed between the predicted cluster labels and the true labels on the test sets and was averaged over 10 performance estimates from the 10-fold cross-validation. Note that K and K' are equal to the number of input strengths ($K = K' = N$ for information differentiation). Higher NMI values indicate greater information differentiation (Fig. 3c).

Supervised framework. In the supervised framework, we utilized the Generalized Linear Model (GLM) to quantify information content in neural signals. The GLM proceeded with three steps: model selection, estimation of model parameters, and prediction (67). Independent simulations across trials satisfied the assumption of independent observations in GLM.

To measure information detection, a GLM was derived separately for each input strength in NREM sleep and all synaptic upscalings in wakefulness. The GLM modeled the true distribution $q(y \mid x,\theta)$, where y represents the response variable (0 for absence of input, 1 for presence of a given input strength), x represents the firing rate of the pyramidal population, and θ represent the model parameters. x consisted of 2×500 values (500 values for spontaneous firing activities and 500 values for evoked firing responses). We employed a Bernoulli distribution due to the binomial nature of the response variable. Stratified 10-fold cross-validation was used to asses the effectiveness of performance of the algorithm. A binomial logistic classification model was fitted on the training sets. The Newton-Raphson iterative optimization technique was carried out to optimize model parameters that maximize the log likelihood function (68, 69). Then, the trained model parameters were used to make predictions on the test sets. Model performance was evaluated using the classification accuracy score as the proportion of correctly predicted samples in the test sets (66). The classification accuracy score was averaged over 10 performance estimates from 10-fold cross-validation. The higher accuracy values indicate greater information detection (Extended Data Fig. 9a(i)).

To measure information differentiation, a GLM was derived separately for NREM sleep and all synaptic upscalings in wakefulness. It modeled the true distribution $q(y \mid x,\theta)$ with y representing the response variable with multiple values ($y \in 0,1,\ldots,N$ for N inputs), x representing the firing rate of the pyramidal population, and θ representing the model parameters. x consisted of $N \times 500$ values, where N is the number of inputs (500 values for evoked firing responses to each input strength). We used the multinomial distribution to estimate model parameters. Stratified 10-fold cross-validation was used to estimate model performance. The Newton-Raphson iterative optimization technique was carried out to optimize model parameters. The trained model parameters were used to estimate the model's performance on the test sets. The classification accuracy score on the test sets was averaged over 10 performance estimates. The higher accuracy values indicate greater information differentiation (Extended Data Fig. 9a(ii)).

Significance Tests and Information Theory.

Significance Test. In a departure from machine learning techniques, we conducted significance tests on firing rate signals from pyramidal populations.

To assess how significantly evoked responses at the input offset differ from spontaneous activities during prestimulus intervals, we employed Student's t-test separately for various input strengths in both NREM sleep and all synaptic upscalings in wakefulness. Given the large number of trials (500 trials), satisfying the conditions of the Central Limit Theorem, we computed the independent t-test statistic (t-value) as follows:

$$t = (\bar{x}_1 - \bar{x}_2)/(s\sqrt{2/n}), \quad \textbf{(29)}$$

$$s^2 = \frac{((n-1)s_1^2 + (n-1)s_2^2)}{2n-1}, \quad \textbf{(30)}$$

DRAFT

Here, $\bar{x}_1$ and $\bar{x}_2$ represent the averages across trials of evoked firing responses at the input offset to a given input strength and spontaneous firing activities at a random time point in prestimulus intervals, respectively. n is the number of trials and $s^2_{1/2}$ is the variance of variable $x_{1/2}$ across trials. We set statistical significance at p-values below 0.05. The *t*-value was used as the measure to quantify the extent to which evoked responses differ from spontaneous activities. A higher *t*-value indicates greater information detection (Extended Data Fig. 9b(i)).

To assess how significantly evoked responses to different input strengths are different from each other, we performed a one-way analysis of variance (ANOVA) separately in NREM sleep and all synaptic upscalings in wakefulness. We computed the F-ratio as follows:

$$\mathrm{F} = \frac{MS_B}{MS_W} \tag{31}$$

where MS_B and MS_W are between-group and within-group mean square values, respectively:

$$MS_B = \frac{\sum_{i=1}^{N} n(\bar{x}_i - \bar{x})}{N-1}, \tag{32}$$

$$MS_W = \frac{\sum_{i=1}^{N}\sum_{j=1}^{n}(x_{i,j} - \bar{x}_i)}{N(n-1)}, \tag{33}$$

Here, N represents the number of inputs, and n is the number of trials. $\bar{x}_{i,j}$ is the evoked firing response to input i in trial j, $\bar{x}_i$ is the average of $\bar{x}_{i,j}$ across trials, and $\bar{x}$ is the average of $\bar{x}_i$ across inputs. The F-ratio was used as the measure to quantify how distinct evoked responses to different input strengths are from each other. A higher F-ratio indicates greater information differentiation (Extended Data Fig. 9b(ii)).

Information Theory. Information theory was also employed to evaluate how informative evoked firing responses at the input offset are about input strengths. Mutual information measures the information about an input in the probability distribution of firing rates, as follows (62):

$$I(X, s_j) = \sum_i p(x_i|s_j)\log_2 \frac{p(x_i|s_j)}{p(x_i)}, \tag{34}$$

Here, $I(X, s_j)$ represents the mutual information between the distribution of firing responses X and input s_j. $p(x_i)$ and $p(x_i|s_j)$ are, respectively, the probability that firing responses take the value x_i and the conditional probability that firing responses take the value x_i for a given input s_j. Summing values of mutual information for all inputs results in a scalar mutual information value $I(X, S)$. A larger separation among the distributions of evoked responses to inputs results in a larger mutual information value. Therefore, a larger mutual information value might represent a higher degree of information differentiation (Extended Data Fig. 9c). Note that to compute mutual information, we discretized firing rate signals into 0.1 Hz bins to calculate the probabilities.

Declarations

Supplementary information. The supplementary information for this paper includes the mathematical formalism for the computational models and extended data Figures.

Funding. This research was funded by the Postdoctoral Junior Leader Fellowship Programme from La Caixa Banking Foundation (LCF/BQ/PI18/11630004) and the Howard Hughes Medical Institute (HHMI ID 55008742).

Competing interests. The authors declare no competing interests. The funders had no role in the design of the study; in the collection, analyses, or interpretation of data; in the writing of the manuscript, or in the decision to publish the results.

Ethics approval. Not applicable

Consent to participate. Not applicable

Consent for publication. Not applicable

Data availability. Datasets supporting the findings of this paper are available in a supplementary information excel file.

Code availability. Code supporting the findings of this paper are available on github.

Authors' contributions. F.R. and B.S. conceived the research. B.S. secured funding. F.R. and B.S. developed the methodology. F.R. designed the simulations and carried out data curation, data analysis, and data visualization. F.R. wrote the original draft. F.R. and B.S. wrote and edited the manuscript. B.S. supervised the research.

Acknowledgment. We thank Francesco Damiani for comments on this manuscript.

DRAFT

Bibliography

1. Karl J. Friston. Functional and effective connectivity in neuroimaging: A synthesis. *Human Brain Mapping*, 2(1-2):56–78, January 1994. doi: 10.1002/hbm.460020107.
2. Marcello Massimini, Fabio Ferrarelli, Reto Huber, Steve K. Esser, Harpreet Singh, and Giulio Tononi. Breakdown of cortical effective connectivity during sleep. *Science*, 309(5744):2228–2232, September 2005. doi: 10.1126/science.1117256.
3. Adenauer G. Casali, Olivia Gosseries, Mario Rosanova, Mélanie Boly, Simone Sarasso, Karina R. Casali, Silvia Casarotto, Marie-Aurélie Bruno, Steven Laureys, Giulio Tononi, and Marcello Massimini. A theoretically based index of consciousness independent of sensory processing and behavior. *Science Translational Medicine*, 5(198), August 2013. ISSN 1946-6242. doi: 10.1126/scitranslmed.3006294.
4. Hanna Hayat, Amit Marmelshtein, Aaron J. Krom, Yaniv Sela, Ariel Tankus, Ido Strauss, Firas Fahoum, Itzhak Fried, and Yuval Nir. Reduced neural feedback signaling despite robust neuron and gamma auditory responses during human sleep. *Nature Neuroscience*, 25(7):935–943, July 2022. doi: 10.1038/s41593-022-01107-4.
5. Thomas E. Scammell, Elda Arrigoni, and Jonathan O. Lipton. Neural circuitry of wakefulness and sleep. *Neuron*, 93(4):747–765, February 2017. doi: 10.1016/j.neuron.2017.01.014.
6. Chiara Cirelli and Giulio Tononi. Differential expression of plasticity-related genes in waking and sleep and their regulation by the noradrenergic system. *The Journal of Neuroscience*, 20(24):9187–9194, December 2000. doi: 10.1523/jneurosci.20-24-09187.2000.
7. Mircea Steriade, David A. McCormick, and Terrence J. Sejnowski. Thalamocortical oscillations in the sleeping and aroused brain. *Science*, 262(5134):679–685, October 1993. doi: 10.1126/science.8235588.
8. M. Steriade, I. Timofeev, and F. Grenier. Natural waking and sleep states: A view from inside neocortical neurons. *Journal of Neurophysiology*, 85(5):1969–1985, May 2001. doi: 10.1152/jn.2001.85.5.1969.
9. H. Davis F. A. Gibbs and W. G. Lennox. The electro encephalogram in epilepsy and in conditions of impaired consciousness. *Archives of Neurology And Psychiatry*, 34(6):1133, December 1935. doi: 10.1001/archneurpsyc.1935.02250240002001.

10. Vladyslav V. Vyazovskiy, Umberto Olcese, Yaniv M. Lazimy, Ugo Faraguna, Steve K. Esser, Justin C. Williams, Chiara Cirelli, and Giulio Tononi. Cortical firing and sleep homeostasis. *Neuron*, 63(6):865–878, September 2009. doi: 10.1016/j.neuron.2009.08.024.
11. Marcello Massimini, Fabio Ferrarelli, Steve K. Esser, Brady A. Riedner, Reto Huber, Michael Murphy, Michael J. Peterson, and Giulio Tononi. Triggering sleep slow waves by transcranial magnetic stimulation. *Proceedings of the National Academy of Sciences*, 104(20):8496–8501, May 2007. doi: 10.1073/pnas.0702495104.
12. Giulio Tononi and Marcello Massimini. Why does consciousness fade in early sleep?. *Annals of the New York Academy of Sciences*, 1129(1):330–334, May 2008. doi: 10.1196/annals.1417.024.
13. Marcello Massimini, Fabio Ferrarelli, Simone Sarasso, and Giulio Tononi. Cortical mechanisms of loss of consciousness: insight from tms/eeg studies. *Archives italiennes de biologie*, 150(2/3):44–55, 2012.
14. Andrea Pigorini, Simone Sarasso, Paola Proserpio, Caroline Szymanski, Gabriele Arnulfo, Silvia Casarotto, Matteo Fecchio, Mario Rosanova, Maurizio Mariotti, Giorgio Lo Russo, J. Matias Palva, Lino Nobili, and Marcello Massimini. Bistability breaks-off deterministic responses to intracortical stimulation during non-REM sleep. *NeuroImage*, 112:105–113, May 2015. doi: 10.1016/j.neuroimage.2015.02.056.
15. Elias B. Issa and Xiaoqin Wang. Sensory responses during sleep in primate primary and secondary auditory cortex. *The Journal of Neuroscience*, 28(53):14467–14480, December 2008. doi: 10.1523/jneurosci.3086-08.2008.
16. Yuval Nir, Vladyslav V. Vyazovskiy, Chiara Cirelli, Matthew I. Banks, and Giulio Tononi. Auditory responses and stimulus-specific adaptation in rat auditory cortex are preserved across NREM and REM sleep. *Cerebral Cortex*, 25(5):1362–1378, December 2013. doi: 10.1093/cercor/bht328.
17. Yaniv Sela, Aaron Joseph Krom, Lottem Bergman, Noa Regev, and Yuval Nir. Sleep differentially affects early and late neuronal responses to sounds in auditory and perirhinal cortices. *The Journal of Neuroscience*, 40(14):2895–2905, February 2020. doi: 10.1523/jneurosci.1186-19.2020.
18. Giulio Tononi and Chiara Cirelli. Sleep function and synaptic homeostasis. *Sleep Medicine Reviews*, 10(1):49–62, February 2006. doi: 10.1016/j.smrv.2005.05.002.
19. Giulio Tononi and Chiara Cirelli. Sleep and the price of plasticity: From synaptic and cellular homeostasis to memory consolidation and integration. *Neuron*, 81(1):12–34, January 2014. doi: 10.1016/j.neuron.2013.12.025.
20. Julian M. Budd and Zoltán F. Kisvárday. Local lateral connectivity of inhibitory clutch cells in layer 4 of cat visual cortex (area 17). *Experimental Brain Research*, 140(2):245–250, July 2001. doi: 10.1007/s002210100817.
21. Péter Buzás, Krisztina Kovács, Alex S. Ferecskó, Julian M.L. Budd, Ulf T. Eysel, and Zoltán F. Kisvárday. Model-based analysis of excitatory lateral connections in the visual cortex. *Journal of Comparative Neurology*, 499(6):861–881, October 2006. doi: 10.1002/cne.21134.
22. Ján Antolík. Rapid long-range disynaptic inhibition explains the formation of cortical orientation maps. *Frontiers in Neural Circuits*, 11, March 2017. doi: 10.3389/fncir.2017.00021.
23. Frances S Chance, L.F Abbott, and Alex D Reyes. Gain modulation from background synaptic input. *Neuron*, 35(4):773–782, August 2002. doi: 10.1016/s0896-6273(02)00820-6.
24. Jeffry S. Isaacson and Massimo Scanziani. How inhibition shapes cortical activity. *Neuron*, 72(2):231–243, October 2011. doi: 10.1016/j.neuron.2011.09.027.
25. R.W. Guillery and S.Murray Sherman. Thalamic relay functions and their role in corticocortical communication. *Neuron*, 33(2):163–175, January 2002. doi: 10.1016/s0896-6273(01)00582-7.
26. Gordon M. G. Shepherd and Naoki Yamawaki. Untangling the cortico-thalamo-cortical loop: cellular pieces of a knotty circuit puzzle. *Nature Reviews Neuroscience*, 22(7):389–406, May 2021. doi: 10.1038/s41583-021-00459-3.
27. Hugh R. Wilson and Jack D. Cowan. Excitatory and inhibitory interactions in localized populations of model neurons. *Biophysical Journal*, 12(1):1–24, January 1972. doi: 10.1016/s0006-3495(72)86068-5.
28. Arne Weigenand, Michael Schellenberger Costa, Hong-Viet Victor Ngo, Jens Christian Claussen, and Thomas Martinetz. Characterization of k-complexes and slow wave activity in a neural mass model. *PLoS Computational Biology*, 10(11):e1003923, November 2014. doi: 10.1371/journal.pcbi.1003923.
29. Farhad Razi, Rubén Moreno-Bote, and Belén Sancristóbal. Computational modeling of information propagation during the sleep–waking cycle. *Biology*, 10(10):945, September 2021. doi: 10.3390/biology10100945.
30. Maria V. Sanchez-Vives and David A. McCormick. Cellular and network mechanisms of rhythmic recurrent activity in neocortex. *Nature Neuroscience*, 3(10):1027–1034, October 2000. doi: 10.1038/79848.
31. Albert Compte, Maria V. Sanchez-Vives, David A. McCormick, and Xiao-Jing Wang. Cellular and network mechanisms of slow oscillatory activity ($<$1 hz) and wave propagations in a cortical network model. *Journal of Neurophysiology*, 89(5):2707–2725, May 2003. doi: 10.1152/jn.00845.2002.
32. Maria V Sanchez-Vives. Origin and dynamics of cortical slow oscillations. *Current Opinion in Physiology*, 15:217–223, June 2020. doi: 10.1016/j.cophys.2020.04.005.
33. Madhura R. Joglekar, Jorge F. Mejias, Guangyu Robert Yang, and Xiao-Jing Wang. Inter-areal balanced amplification enhances signal propagation in a large-scale circuit model of the primate cortex. *Neuron*, 98(1):222–234.e8, April 2018. doi: 10.1016/j.neuron.2018.02.031.
34. Gustavo Deco, Yonathan Sanz Perl, Peter Vuust, Enzo Tagliazucchi, Henry Kennedy, and Morten L. Kringelbach. Rare long-range cortical connections enhance human information processing. *Current Biology*, 31(20):4436–4448.e5, October 2021. doi: 10.1016/j.cub.2021.07.064.
35. Leslie D Claar, Irene Rembado, Jacqulyn R Kuyat, Simone Russo, Lydia C Marks, Shawn R Olsen, and Christof Koch. Cortico-thalamo-cortical interactions modulate electrically evoked EEG responses in mice. *eLife*, 12, June 2023. doi: 10.7554/elife.84630.3.
36. David A. McCormick. Cholinergic and noradrenergic modulation of thalamocortical processing. *Trends in Neurosciences*, 12(6):215–221, January 1989. doi: 10.1016/0166-2236(89)90125-2.
37. David A McCormick and Thierry Bal. Sensory gating mechanisms of the thalamus. *Current Opinion in Neurobiology*, 4(4):550–556, August 1994. doi: 10.1016/0959-4388(94)90056-6.
38. S. Murray Sherman and R. W. Guillery. The role of the thalamus in the flow of information to the cortex. *Philosophical Transactions of the Royal Society of London. Series B: Biological Sciences*, 357(1428):1695–1708, December 2002. doi: 10.1098/rstb.2002.1161.
39. Mattia D'Andola, Beatriz Rebollo, Adenauer G Casali, Julia F Weinert, Andrea Pigorini, Rosa Villa, Marcello Massimini, and Maria V Sanchez-Vives. Bistability, causality, and complexity in cortical networks: An in vitro perturbational study. *Cerebral Cortex*, 28(7):2233–2242, May 2017. doi: 10.1093/cercor/bhx122.
40. Pascal Fries. A mechanism for cognitive dynamics: neuronal communication through neuronal coherence. *Trends in Cognitive Sciences*, 9(10):474–480, October 2005. doi: 10.1016/j.tics.2005.08.011.
41. Pascal Fries. Rhythms for cognition: Communication through coherence. *Neuron*, 88(1):220–235, October 2015. doi: 10.1016/j.neuron.2015.09.034.
42. Mor Regev, Erez Simony, Katherine Lee, Kean Ming Tan, Janice Chen, and Uri Hasson. Propagation of information along the cortical hierarchy as a function of attention while reading and listening to stories. *Cerebral Cortex*, 29(10):4017–4034, November 2018. doi: 10.1093/cercor/bhy282.
43. Marcel Adam Just, Patricia A. Carpenter, Timothy A. Keller, William F. Eddy, and Keith R. Thulborn. Brain activation modulated by sentence comprehension. *Science*, 274(5284):114–116, October 1996. doi: 10.1126/science.274.5284.114.
44. Chiara Cirelli and Giulio Tononi. Effects of sleep and waking on the synaptic ultrastructure. *Philosophical Transactions of the Royal Society B: Biological Sciences*, 375(1799):20190235, April 2020. doi: 10.1098/rstb.2019.0235.
45. Mark S. Cembrowski and Nelson Spruston. Heterogeneity within classical cell types is the rule: lessons from hippocampal pyramidal neurons. *Nature Reviews Neuroscience*, 20(4):193–204, February 2019. doi: 10.1038/s41583-019-0125-5.
46. Nelson Spruston. Pyramidal neurons: dendritic structure and synaptic integration. *Nature Reviews Neuroscience*, 9(3):206–221, March 2008. doi: 10.1038/nrn2286.
47. Matthew E. Larkum, J. Julius Zhu, and Bert Sakmann. A new cellular mechanism for coupling inputs arriving at different cortical layers. *Nature*, 398(6725):338–341, March 1999. doi: 10.1038/18686.
48. Hannah Monyer, Nail Burnashev, David J. Laurie, Bert Sakmann, and Peter H. Seeburg. Developmental and regional expression in the rat brain and functional properties of four NMDA receptors. *Neuron*, 12(3):529–540, March 1994. doi: 10.1016/0896-6273(94)90210-0.
49. Olivier David and Karl J. Friston. A neural mass model for MEG/EEG:. *NeuroImage*, 20(3):1743–1755, November 2003. doi: 10.1016/j.neuroimage.2003.07.015.
50. Steve K. Esser, Sean Hill, and Giulio Tononi. Breakdown of effective connectivity during slow wave sleep: Investigating the mechanism underlying a cortical gate using large-scale modeling. *Journal of Neurophysiology*, 102(4):2096–2111, October 2009. doi: 10.1152/jn.00059.2009.
51. G. Deco, A. Ponce-Alvarez, P. Hagmann, G. L. Romani, D. Mantini, and M. Corbetta. How local excitation-inhibition ratio impacts the whole brain dynamics. *Journal of Neuroscience*, 34(23):7886–7898, June 2014. doi: 10.1523/jneurosci.5068-13.2014.
52. Benjamin P. Cohen, Carson C. Chow, and Shashaank Vattikuti. Dynamical modeling of multi-scale variability in neuronal competition. *Communications Biology*, 2(1), August 2019. doi: 10.1038/s42003-019-0555-7.
53. Almudena Barbero-Castillo, Pedro Mateos-Aparicio, Leonardo Dalla Porta, Alessandra Camassa, Lorena Perez-Mendez, and Maria V. Sanchez-Vives. Impact of $GABA_a$ and $GABA_b$ inhibition on cortical dynamics and perturbational complexity during synchronous and desynchronized states. *The Journal of Neuroscience*, 41(23):5029–5044, April 2021. doi: 10.1523/jneurosci.1837-20.2021.
54. Jennifer S. Goldman, Lionel Kusch, David Aquilue, Bahar Hazal Yalçınkaya, Damien Depannemaecker, Kevin Ancourt, Trang-Anh E. Nghiem, Viktor Jirsa, and Alain Destexhe. A comprehensive neural simulation of slow-wave sleep and highly responsive wakefulness dynamics. *Frontiers in Computational Neuroscience*, 16, January 2023. doi: 10.3389/fncom.2022.1058957.
55. Wulfram Gerstner, Werner M Kistler, Richard Naud, and Liam Paninski. *Neuronal dynamics: From single neurons to networks and models of cognition*. Cambridge University Press, 2014.
56. A. L. Hodgkin, A. F. Huxley, and B. Katz. Measurement of current-voltage relations in the membrane of the giant axon of $loligo$. *The Journal of Physiology*, 116(4):424–448, April 1952. doi: 10.1113/jphysiol.1952.sp004716.
57. Alain Destexhe, Stuart W. Hughes, Michelle Rudolph, and Vincenzo Crunelli. Are corticothalamic 'up' states fragments of wakefulness? *Trends in Neurosciences*, 30(7):334–342, July 2007. doi: 10.1016/j.tins.2007.04.006.
58. Maxi San Miguel and Raúl Toral. *Stochastic Effects in Physical Systems*, pages 35–127. Springer Netherlands, Dordrecht, 2000. ISBN 978-94-011-4247-2. doi: 10.1007/978-94-011-4247-2_2.
59. Walter J. Freeman and Rodrigo Quian Quiroga. *Imaging Brain Function With EEG*. Springer New York, 2013. doi: 10.1007/978-1-4614-4984-3.
60. P. Welch. The use of fast fourier transform for the estimation of power spectra: A method based on time averaging over short, modified periodograms. *IEEE Transactions on Audio and Electroacoustics*, 15(2):70–73, June 1967. doi: 10.1109/tau.1967.1161901.
61. Wulfram Gerstner, Andreas K. Kreiter, Henry Markram, and Andreas V. M. Herz. Neural codes: Firing rates and beyond. *Proceedings of the National Academy of Sciences*, 94(24):12740–12741, November 1997. doi: 10.1073/pnas.94.24.12740.
62. Alexander Borst and Frédéric E. Theunissen. Information theory and neural coding. *Nature Neuroscience*, 2(11):947–957, November 1999. doi: 10.1038/14731.
63. Giulio Tononi, Melanie Boly, Marcello Massimini, and Christof Koch. Integrated information theory: from consciousness to its physical substrate. *Nature Reviews Neuroscience*, 17(7):450–461, May 2016. doi: 10.1038/nrn.2016.44.
64. Alexander Strehl and Joydeep Ghosh. Cluster ensembles—a knowledge reuse framework for combining multiple partitions. *Journal of machine learning research*, 3(Dec):583–617, 2002.
65. Marina Meilă. Comparing clusterings—an information based distance. *Journal of Multivari-*

DRAFT

ate Analysis, 98(5):873–895, May 2007. doi: 10.1016/j.jmva.2006.11.013.
66. Max Kuhn, Kjell Johnson, et al. *Applied predictive modeling*, volume 26. Springer, 2013.
67. P. McCullagh and J.A. Nelder. *Generalized Linear Models*. Routledge, January 2019. doi: 10.1201/9780203753736.
68. Christopher M Bishop and Nasser M Nasrabadi. *Pattern recognition and machine learning*, volume 4. Springer, 2006.
69. Stephen P Boyd and Lieven Vandenberghe. *Convex optimization*. Cambridge university press, 2004.

DRAFT

Appendix A: The Mathematical Formalism for the Computational Models

The mathematical formalism for the computational models have been previously described in our earlier work (29).

One-Cortical-Column Model. The one-cortical-column model consists of one pyramidal and one inhibitory population. The model utilizes the mathematical formalism of the Hodgkin-Huxley model to describe the membrane voltage activity in terms of driving synaptic activity. The synaptic activity contains one leak, two synaptic (intra-AMPAergic and GABAergic) currents, and one activity-dependent potassium current.

In the absence of Gaussian noise for the set of parameters in Table 2, the system relaxes to the steady-state solution. However, at every time point, the Gaussian noise disrupts the system from the steady-state solution. Nevertheless, the aforementioned synaptic currents drive the system back to the steady-state solution.

The full model equations for the one-cortical-column model are described by:

$$\begin{aligned}
\tau_p \dot{V}_p &= -I_{\mathrm{L}}^p - I_{intra\text{-AMPA}}^p - I_{\mathrm{GABA}}^p - \tau_p C_m^{-1} I_{\mathrm{KNa}}, \\
\tau_i \dot{V}_i &= -I_{\mathrm{L}}^i - I_{intra\text{-AMPA}}^i - I_{\mathrm{GABA}}^i,
\end{aligned}$$

$$\begin{aligned}
\ddot{s}_{pp} &= \gamma_p^2 \left(N_{pp}\, Q_p(V_p) + \phi_p - s_{pp}\right) - 2\gamma_p\, \dot{s}_{pp}, \\
\ddot{s}_{pi} &= \gamma_i^2 \left(N_{pi}\, Q_i(V_i) - s_{pi}\right) - 2\gamma_i\, \dot{s}_{pi}, \\
\ddot{s}_{ip} &= \gamma_p^2 \left(N_{ip}\, Q_p(V_p) + \phi_i - s_{ip}\right) - 2\gamma_p\, \dot{s}_{ip}, \\
\ddot{s}_{ii} &= \gamma_i^2 \left(N_{ii}\, Q_i(V_i) - s_{ii}\right) - 2\gamma_i\, \dot{s}_{ii},
\end{aligned}$$

$$\tau_{\mathrm{Na}}\, [\dot{\mathrm{Na}}] = \alpha_{\mathrm{Na}} Q_p(V_p) - \mathrm{Na}_{\mathrm{pump}}([\mathrm{Na}]),$$

with the currents defined by:

$$\begin{aligned}
I_{\mathrm{L}}^k &= \bar{g}_{\mathrm{L}}(V_k - E_{\mathrm{L}}^k), \\
I_{\mathrm{AMPA}}^k &= \beta_{intra}\, \bar{g}_{\mathrm{AMPA}} s_{kp}(V_k - E_{\mathrm{AMPA}}), \\
I_{\mathrm{GABA}}^k &= \beta_{\mathrm{GABA}}^k\, \bar{g}_{\mathrm{GABA}} s_{ki}(V_k - E_{\mathrm{GABA}}), \\
I_{\mathrm{KNa}} &= \bar{g}_{\mathrm{KNa}} \frac{0.37}{1 + (\frac{38.7}{[\mathrm{Na}]})^{3.5}} (V_p - E_{\mathrm{K}}),\ \textit{for}\ k \in \{p,\, i\},
\end{aligned}$$

The sodium pump and the firing rate functions are given by:

$$\begin{aligned}
\mathrm{Na}_{\mathrm{pump}}([\mathrm{Na}]) &= R_{\mathrm{pump}} \left(\frac{[\mathrm{Na}]^3}{[\mathrm{Na}]^3 + 3375} - \frac{[\mathrm{Na}]_{\mathrm{eq}}^3}{[\mathrm{Na}]_{\mathrm{eq}}^3 + 3375} \right), \\
Q_k(V_k) &= Q_k^{max} \frac{(1 + \tanh(C(V_k - \theta_k)/\sigma_k))}{2}, \quad C = \frac{\pi}{2\sqrt{3}},\ \textit{for}\ k \in \{p,\, i\},
\end{aligned}$$

Dynamical Constrains on β_{GABA}^k in the One-Cortical-Column Model. Upscaling the average conductance of intra-excitatory connections by a factor β_{intra} allows us to transition the model from NREM sleep dynamics to wakefulness, in agreement with SHY. To counterbalance the overexcitation each population receives due to intra-synaptic upscaling, the average GABAergic conductance on pyramidal and inhibitory populations is increased by a factor β_{GABA}^k, where $k \in \{p,\, i\}$. To do so, we use the peaks of V_p and V_i values during Up states in NREM sleep as the steady-state value of the average membrane potential of pyramidal and inhibitory populations in wakefulness. β_{GABA}^k is increased until the value of V_k (where $k \in \{p,\, i\}$) is obtained for various intra-synaptic upscalings in wakefulness.

The steady-state solution of the model equations in the one-cortical-column model (see Appendix) is obtained by setting the derivative of all variables to zero:

DRAFT

$$
\begin{aligned}
0 &= -I_{\mathrm{L}}^{p} - I_{intra\text{-AMPA}}^{p} - I_{\mathrm{GABA}}^{p} - \tau_p C_m^{-1} I_{\mathrm{KNa}}, \\
0 &= -I_{\mathrm{L}}^{i} - I_{intra\text{-AMPA}}^{i} - I_{\mathrm{GABA}}^{i}, \\
s_{kk'} &= N_{kk'}\, Q_{k'}(V_{k'}), \\
[\mathrm{Na}] &= \sqrt[3]{\frac{\mathrm{A}\cdot 3375}{1-\mathrm{A}}}, \\
\mathrm{A} &= \frac{\alpha_{\mathrm{Na}}}{R_{\mathrm{pump}}} Q_p(V_p) + \frac{[\mathrm{Na}]_{\mathrm{eq}}^3}{[\mathrm{Na}]_{\mathrm{eq}}^3 + 3375},
\end{aligned}
$$

Therefore, $\beta_{\mathrm{GABA}}^{k}$, $k \in \{p,\ i\}$ is as follows:

$$
\beta_{\mathrm{GABA}}^{p} = \frac{-\bar{g}_{\mathrm{L}}(V_p - E_{\mathrm{L}}^{p}) - \beta_{intra}\ \bar{g}_{\mathrm{AMPA}}\ s_{pp}(V_p - E_{\mathrm{AMPA}})}{\bar{g}_{\mathrm{GABA}}\ s_{pi}(V_p - E_{\mathrm{GABA}})}
$$

$$
+ \frac{-\bar{g}_{\mathrm{KNa}}\ \dfrac{0.37}{1+(\frac{38.7}{[\mathrm{Na}]})^{3.5}}\,(V_p - E_{\mathrm{K}})}{\bar{g}_{\mathrm{GABA}}\ s_{pi}(V_p - E_{\mathrm{GABA}})},
$$

$$
\beta_{\mathrm{GABA}}^{i} = \frac{-\bar{g}_{\mathrm{L}}(V_i - E_{\mathrm{L}}^{i}) - \beta_{intra}\ \bar{g}_{\mathrm{AMPA}} s_{ip}(V_i - E_{\mathrm{AMPA}})}{\bar{g}_{\mathrm{GABA}}\ s_{ii}(V_i - E_{\mathrm{GABA}})},
$$

$\beta_{\mathrm{GABA}}^{k}$, where $k \in \{p,\ i\}$, for a given intra-synaptic upscaling in wakefulness is obtained by substituting the corresponding β_{intra} and the peaks of V_p and V_i values during Up states in NREM sleep.

Two-Cortical-Column Model. The two-cortical-column model consists of two cortical columns each containing one pyramidal and one inhibitory population (Appendix) that are mutually coupled through inter-excitatory connections. Full model equations for the two-cortical-column model are described by:

DRAFT

$$\tau_p \dot{V}_p = -I_{\mathrm{L}}^p - I_{intra\text{-AMPA}}^p - I_{inter\text{-AMPA}}^p - I_{\mathrm{GABA}}^p - \tau_p C_m^{-1} I_{\mathrm{KNa}}^p,$$
$$\tau_i \dot{V}_i = -I_{\mathrm{L}}^i - I_{intra\text{-AMPA}}^i - I_{inter\text{-AMPA}}^i - I_{\mathrm{GABA}}^i,$$

$$\tau_{p'} \dot{V}_{p'} = -I_{\mathrm{L}}^{p'} - I_{intra\text{-AMPA}}^{p'} - I_{inter\text{-AMPA}}^{p'} - I_{\mathrm{GABA}}^{p'} - \tau_{p'} C_m^{-1} I_{\mathrm{KNa}}^{p'},$$
$$\tau_{i'} \dot{V}_{i'} = -I_{\mathrm{L}}^{i'} - I_{intra\text{-AMPA}}^{i'} - I_{inter\text{-AMPA}}^{i'} - I_{\mathrm{GABA}}^{i'},$$

$$\ddot{s}_{pp} = \gamma_p^2 \left(N_{pp}\, Q_p(V_p) + \phi_p - s_{pp}\right) - 2\gamma_p\, \dot{s}_{pp},$$
$$\ddot{s}_{pi} = \gamma_i^2 \left(N_{pi}\, Q_i(V_i) - s_{pi}\right) - 2\gamma_i\, \dot{s}_{pi},$$
$$\ddot{s}_{ip} = \gamma_p^2 \left(N_{ip}\, Q_p(V_p) + \phi_i - s_{ip}\right) - 2\gamma_p\, \dot{s}_{ip},$$
$$\ddot{s}_{ii} = \gamma_i^2 \left(N_{ii}\, Q_i(V_i) - s_{ii}\right) - 2\gamma_i\, \dot{s}_{ii},$$

$$\ddot{s}_{p'p'} = \gamma_{p'}^2 \left(N_{p'p'}\, Q_{p'}(V_{p'}) + \phi_{p'} - s_{p'p'}\right) - 2\gamma_{p'}\, \dot{s}_{p'p'},$$
$$\ddot{s}_{p'i'} = \gamma_{i'}^2 \left(N_{p'i'}\, Q_{i'}(V_{i'}) - s_{p'i'}\right) - 2\gamma_{i'}\, \dot{s}_{p'i'},$$
$$\ddot{s}_{i'p'} = \gamma_{p'}^2 \left(N_{i'p'}\, Q_{p'}(V_{p'}) + \phi_{i'} - s_{i'p'}\right) - 2\gamma_{p'}\, \dot{s}_{i'p'},$$
$$\ddot{s}_{i'i'} = \gamma_{i'}^2 \left(N_{i'i'}\, Q_{i'}(V_{i'}) - s_{i'i'}\right) - 2\gamma_{i'}\, \dot{s}_{i'i'},$$

$$\ddot{s}_{pp'} = \gamma_{p'}^2 \left(N_{pp'}\, Q_{p'}(V_{p'}) - s_{pp'}\right) - 2\gamma_{p'}\, \dot{s}_{pp'},$$
$$\ddot{s}_{ip'} = \gamma_{p'}^2 \left(N_{ip'}\, Q_{p'}(V_{p'}) - s_{ip'}\right) - 2\gamma_{p'}\, \dot{s}_{ip'},$$

$$\ddot{s}_{p'p} = \gamma_p^2 \left(N_{p'p}\, Q_p(V_p) - s_{p'p}\right) - 2\gamma_p\, \dot{s}_{p'p},$$
$$\ddot{s}_{i'p} = \gamma_p^2 \left(N_{i'p}\, Q_p(V_p) - s_{i'p}\right) - 2\gamma_p\, \dot{s}_{i'p},$$

$$\tau_{\mathrm{Na}}\, [\dot{\mathrm{Na}}]_p = \alpha_{\mathrm{Na}} Q_p(V_p) - \mathrm{Na}_{\mathrm{pump}}([\mathrm{Na}]_p),$$
$$\tau_{\mathrm{Na}}\, [\dot{\mathrm{Na}}]_{p'} = \alpha_{\mathrm{Na}} Q_{p'}(V_{p'}) - \mathrm{Na}_{\mathrm{pump}}([\mathrm{Na}]_{p'}),$$

where I_{KNa}^h is the sodium-dependent potassium current of the pyramidal population either in the first and second cortical column, $h \in \{p, p'\}$. The currents are defined by:

$$I_{\mathrm{L}}^k = \bar{g}_{\mathrm{L}}(V_k - E_{\mathrm{L}}^k),\ \textit{for}\ k \in \{p,\ i,\ p',\ i'\},$$

$$I_{intra\text{-AMPA}}^k = \beta_{intra}\ \bar{g}_{\mathrm{AMPA}}\ s_{kp}\ (V_k - E_{\mathrm{AMPA}})$$
$$I_{inter\text{-AMPA}}^k = \beta_{inter}\ \bar{g}_{\mathrm{AMPA}}\ s_{kp'}\ (V_k - E_{\mathrm{AMPA}})$$
$$I_{\mathrm{GABA}}^k = \beta_{\mathrm{GABA}}^k\ \bar{g}_{\mathrm{GABA}} s_{ki}(V_k - E_{\mathrm{GABA}}),\ \textit{for}\ k \in \{p,\ i\},$$

$$I_{intra\text{-AMPA}}^k = \beta_{intra}\ \bar{g}_{\mathrm{AMPA}}\ s_{kp'}\ (V_k - E_{\mathrm{AMPA}})$$
$$I_{inter\text{-AMPA}}^k = \beta_{inter}\ \bar{g}_{\mathrm{AMPA}}\ s_{kp}\ (V_k - E_{\mathrm{AMPA}})$$
$$I_{\mathrm{GABA}}^k = \beta_{\mathrm{GABA}}^k\ \bar{g}_{\mathrm{GABA}} s_{ki'}(V_k - E_{\mathrm{GABA}}),\ \textit{for}\ k \in \{p',\ i'\},$$

$$I_{\mathrm{KNa}}^h = \bar{g}_{\mathrm{KNa}}\ \frac{0.37}{1 + (\frac{38.7}{[\mathrm{Na}]_h})^{3.5}}\ (V_h - E_{\mathrm{K}}),\ \textit{for}\ h \in \{p,\ p'\},$$

The sodium pump and firing rate functions are given by:

DRAFT

$$\mathrm{Na}_{\mathrm{pump}}([\mathrm{Na}]_h) = R_{\mathrm{pump}}\left(\frac{[\mathrm{Na}]_h^3}{[\mathrm{Na}]_h^3+3375} - \frac{[\mathrm{Na}]_{\mathrm{eq}}^3}{[\mathrm{Na}]_{\mathrm{eq}}^3+3375}\right), \textit{for } h \in \{p,\, p'\},$$

$$Q_k(V_k) = Q_k^{max}\,\frac{(1+\tanh(C(V_k-\theta_k)/\sigma_k))}{2}, \quad C = \frac{\pi}{2\sqrt{3}}, \textit{for } k \in \{p,\, i,\, p',\, i'\},$$

Dynamical Constrains on β^k_{GABA} in the Two-Cortical-Column Model. Inter-excitatory connections introduce overexcitation to the pyramidal and inhibitory populations in NREM sleep. To keep the steady-state value of V_p and V_i in the two-cortical-column model equal to the ones in the one-cortical-column model in NREM sleep, β^k_{GABA}, where $k \in \{p,\, i,\, p',\, i'\}$, is increased to counterbalance the the effects of inter-excitatory connections. The same procedure is carried out for all synaptic upscalings in wakefulness, except that the values of V_p and V_i during Up state in NREM sleep in the one-cortical-column model is used. The steady-state solution of the model equations for the two-cortical-column (see Appendix) is obtained by setting the derivatives of all variables to zero:

$$\begin{aligned}
0 &= -I_{\mathrm{L}}^{p/p'} - I_{\mathrm{AMPA}}^{p/p'} - I_{\mathrm{GABA}}^{p/p'} - \tau_{p/p'} C_m^{-1} I_{\mathrm{KNa}}^{p/p'},\\
0 &= -I_{\mathrm{L}}^{i/i'} - I_{\mathrm{AMPA}}^{i/i'} - I_{\mathrm{GABA}}^{i/i'},\\
s_{kk'} &= N_{kk'}\, Q_{k'}(V_{k'}),\\
s_{kk'} &= N_{kk'}\, Q_{k'}(V_{k'})\\
[\mathrm{Na}]_{p/p'} &= \sqrt[3]{\frac{\mathrm{A}_{p/p'}\cdot 3375}{1-\mathrm{A}_{p/p'}}},\\
\mathrm{A}_{p/p'} &= \frac{\alpha_{\mathrm{Na}}}{R_{\mathrm{pump}}} Q_{p/p'}(V_{p/p'}) + \frac{[\mathrm{Na}]_{\mathrm{eq}}^3}{[\mathrm{Na}]_{\mathrm{eq}}^3+3375},
\end{aligned}$$

By taking into account the symmetry between the two cortical columns, we set the steady-state value of V_p equal to $V_{p'}$ and V_i equal to $V_{i'}$ ($V_{p'} = V_p$ and $V_{i'} = V_i$). Therefore, to keep the average membrane potential of pyramidal and inhibitory populations in the two-cortical-column model equal to the ones in the one-cortical-column model both during NREM sleep and wakefulness, β^k_{GABA}, where $k \in \{p,\, i,\, p',\, i'\}$, changes as follows:

$$\beta_{\mathrm{GABA}}^{p/p'} = \frac{-\bar{g}_{\mathrm{L}}(V_p - E_{\mathrm{L}}^p) - \beta_{intra}\,\bar{g}_{\mathrm{AMPA}}\, s_{pp}(V_p - E_{\mathrm{AMPA}})}{\bar{g}_{\mathrm{GABA}}\, s_{pi}(V_p - E_{\mathrm{GABA}})}$$

$$+ \frac{-\beta_{inter}\,\bar{g}_{\mathrm{AMPA}}\, s_{pp'}(V_p - E_{\mathrm{AMPA}})}{\bar{g}_{\mathrm{GABA}}\, s_{pi}(V_p - E_{\mathrm{GABA}})}$$

$$+ \frac{-\bar{g}_{\mathrm{KNa}}\,\dfrac{0.37}{1+(\frac{38.7}{[\mathrm{Na}]})^{3.5}}\,(V_p - E_{\mathrm{K}})}{\bar{g}_{\mathrm{GABA}}\, s_{pi}(V_p - E_{\mathrm{GABA}})},$$

$$\beta_{\mathrm{GABA}}^{i/i'} = \frac{-\bar{g}_{\mathrm{L}}(V_i - E_{\mathrm{L}}^i) - \beta_{intra}\,\bar{g}_{\mathrm{AMPA}} s_{ip}(V_i - E_{\mathrm{AMPA}})}{\bar{g}_{\mathrm{GABA}}\, s_{ii}(V_i - E_{\mathrm{GABA}})}$$

$$+ \frac{-\beta_{inter}\,\bar{g}_{\mathrm{AMPA}}\, s_{ip'}(V_i - E_{\mathrm{AMPA}})}{\bar{g}_{\mathrm{GABA}}\, s_{ii}(V_i - E_{\mathrm{GABA}})},$$

β^k_{GABA}, where $k \in \{p,\, i,\, p',\, i'\}$, during NREM sleep in the two-cortical-column model is obtained by setting $\beta_{\mathrm{intra}} = \beta_{\mathrm{inter}} = 1$ and using the steady-state values of V_p and V_i in NREM sleep from the one-cortical-column model.

DRAFT

β^k_{GABA}, where $k \in \{p,\, i,\, p',\, i'\}$, for a given synaptic upscaling during wakefulness in the two-cortical-column model is obtained by substituting the corresponding β_{intra} and β_{inter} values and the peaks of V_p and V_i during Up states in NREM sleep from the one-cortical-column model.

DRAFT

Extended Data Figures

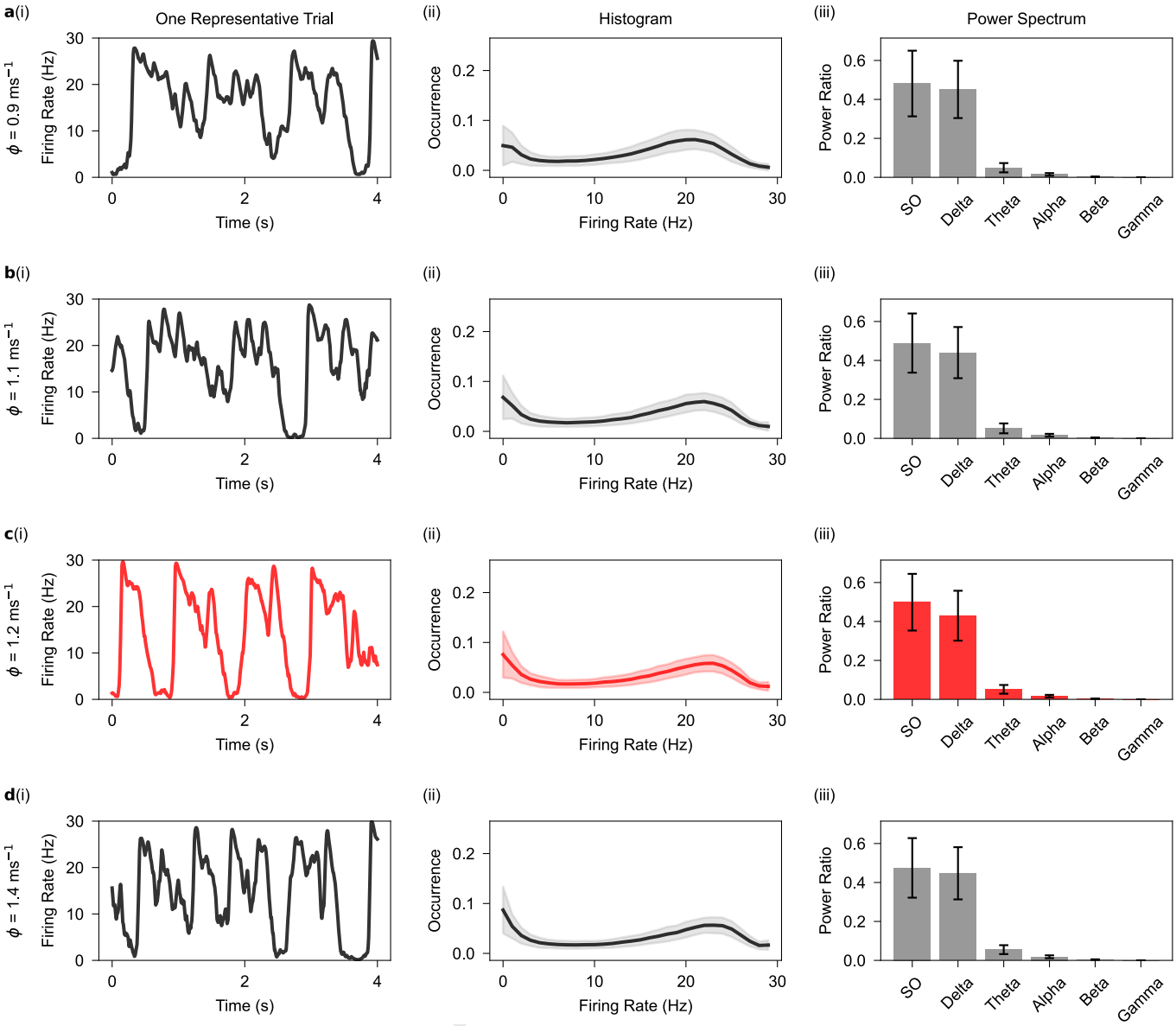

Extended Data Fig. 1. Dynamical features of spontaneous firing activity in the one-cortical-column model are robust to the changes in the standard deviation of the noise, ϕ. a, Spontaneous firing rate signal for a representative trial (i), the distribution of firing rate signals (ii), and the power spectrum of signals (iii) when $\phi = 0.9$ ms^{-1}. **b**, **c**, and **d**, As in **a**, but for when ϕ increases. Panel **c** here is as Fig. 1**c**. Note that $\phi = 1.2$ ms^{-1} is used as the value of the standard deviation of the noise in this computational study. Shaded area and Error bar correspond to standard deviation over 500 trials.

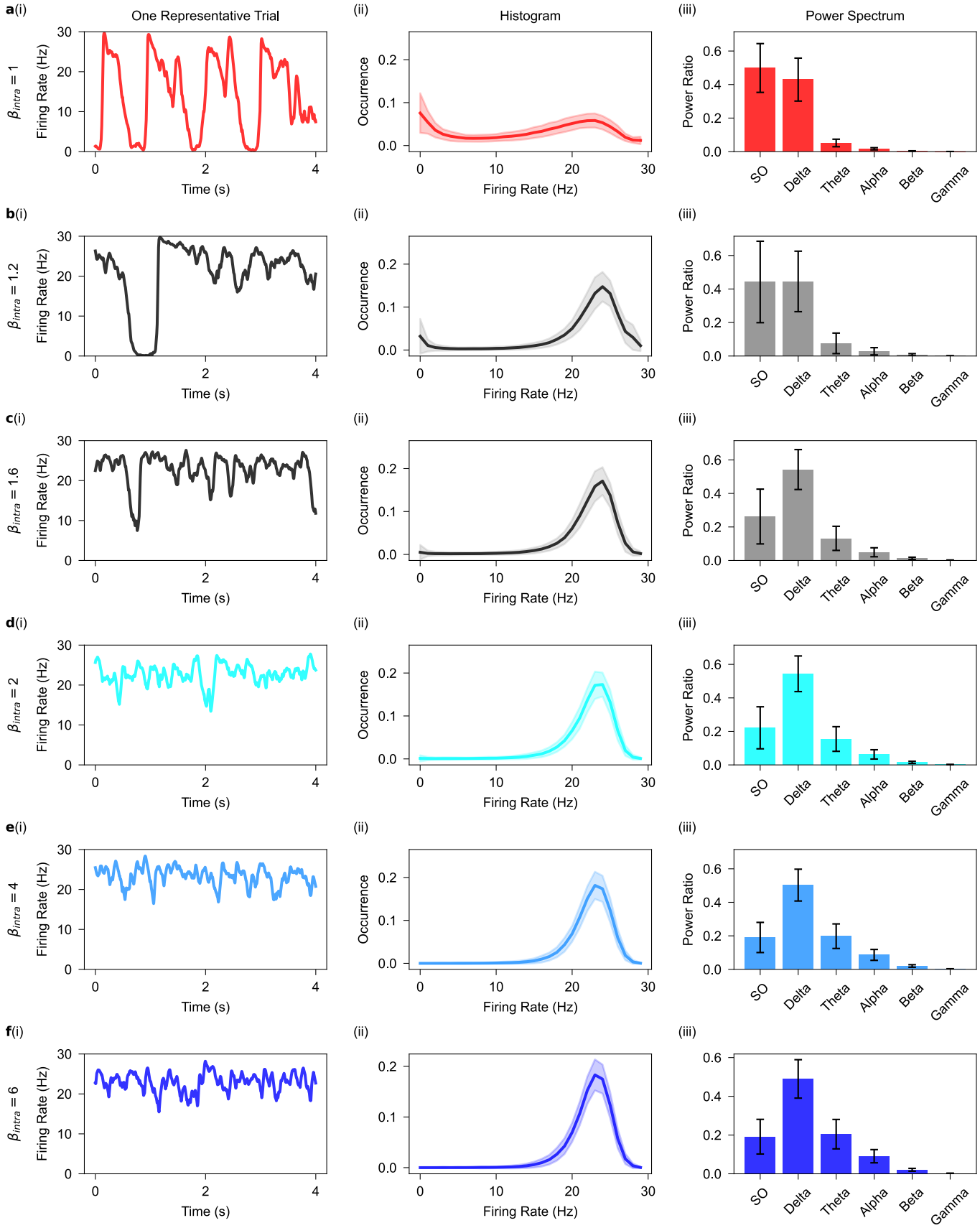

Extended Data Fig. 2. Dynamical features of spontaneous firing activity in the one-cortical-column model changes with increasing intra-synaptic upscaling, β_{intra}. **a**, Spontaneous firing rate signal for a representative trial (i), the distribution of firing rate signals (ii), and the power spectrum of signals (iii) when there is no intra-synaptic upscaling ($\beta_{intra} = 1$). Panel **a** here is as Fig. 1**c**. **b**, **c**, **d**, **e**, and **f**, As in **a**, but for when intra-synaptic upscaling (β_{intra}) increases. Panel **d** here is as Fig. 1**d**. Shaded area and Error bar correspond to standard deviation over 500 trials.

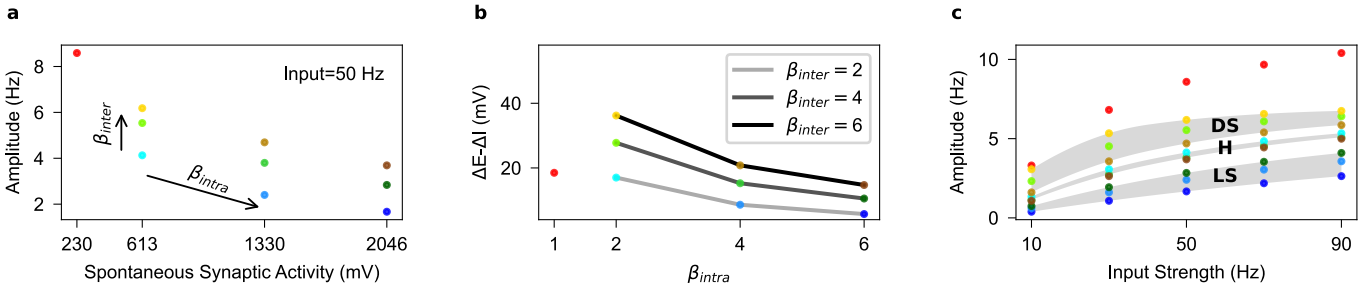

Extended Data Fig. 3. Effect of intra- and inter-synaptic upscaling on the response of one-cortical-column model to inputs. **a**, Increasing spontaneous synaptic activity ($|E| + |I|$) results in decreasing the amplitude of evoked responses when input strength is 50Hz. This holds true for other values of input strength (not shown here). Note that spontaneous synaptic activity increases with increasing intra-synaptic upscaling in the one-cortical-column model. On the other hand, inter-synaptic upscaling does not modulate the spontaneous synaptic activity as it is implicated in the dynamics only during transient input application. **b**, Inter-synaptic upscaling increases the net evoked synaptic current ($\Delta E - \Delta I$), as opposed to when intra-synaptic upscaling increases in wakefulness. **c**, The amplitude of evoked responses to inputs enhances as synaptic upscaling transition from local-selective (LS) towards distance-selective (DS) upscaling during wakefulness.

DRAFT

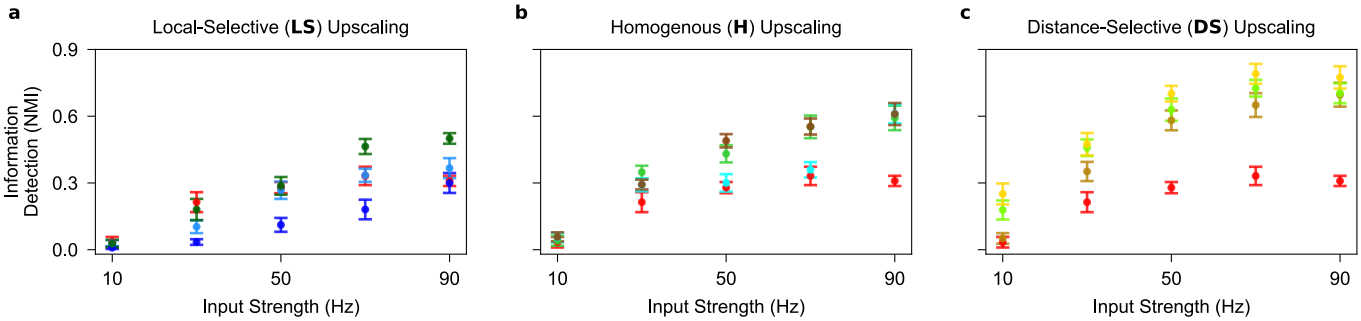

Extended Data Fig. 4. Information detection in the one-cortical-column model. **a**, Information detection for inputs with increasing input strength in NREM sleep and wakefulness, when synaptic upscaling in wakefulness is local-selective upscaling (LS). **b**, and **c**, As in **a**, but for when synaptic upscaling in wakefulness is homogeneous (H) and distance-selective (DS) upscaling, respectively. Error bar corresponds to 95% confidence interval over 10 performance estimate of the K-means clustering algorithms.

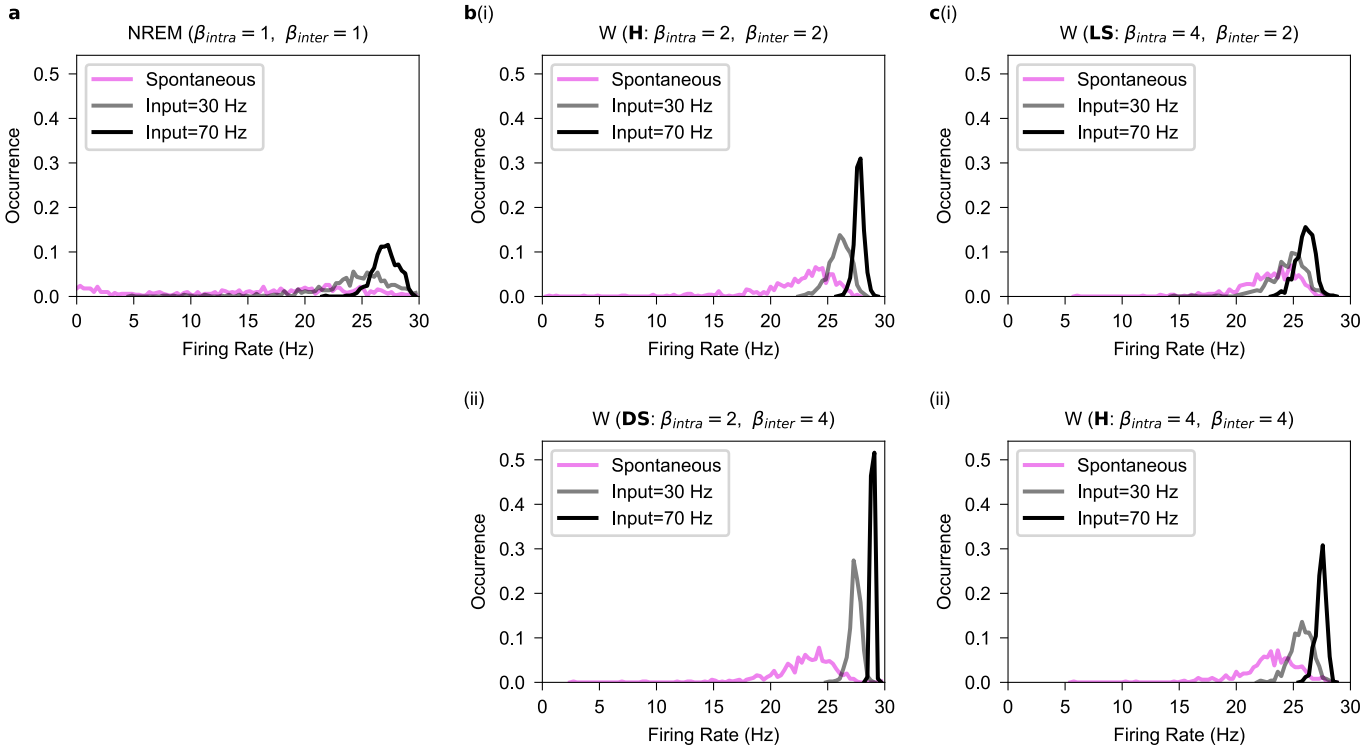

Extended Data Fig. 5. The distribution of spontaneous and evoked firing signals in the one-cortical-column model. **a**, The distribution of spontaneous firing activities and evoked firing responses to inputs with input strength of 30Hz and 70Hz during NREM sleep. **b**, As in **a**, but for wakefulness when $\beta_{intra} = 2,\ \beta_{inter} = 2$ (i) and $\beta_{intra} = 2,\ \beta_{inter} = 4$ (ii). Inter-synaptic upscaling makes the distributions more separable resulting in enhanced information detection and information differentiation during wakefulness. **c**, As in **b**, but for when $\beta_{intra} = 4,\ \beta_{inter} = 2$ (i) and $\beta_{intra} = 4,\ \beta_{inter} = 4$ (ii). Note that intra-synaptic upscaling from b(i) to c(i) makes the distributions less separable resulting in decreased information detection and information differentiation during wakefulness.

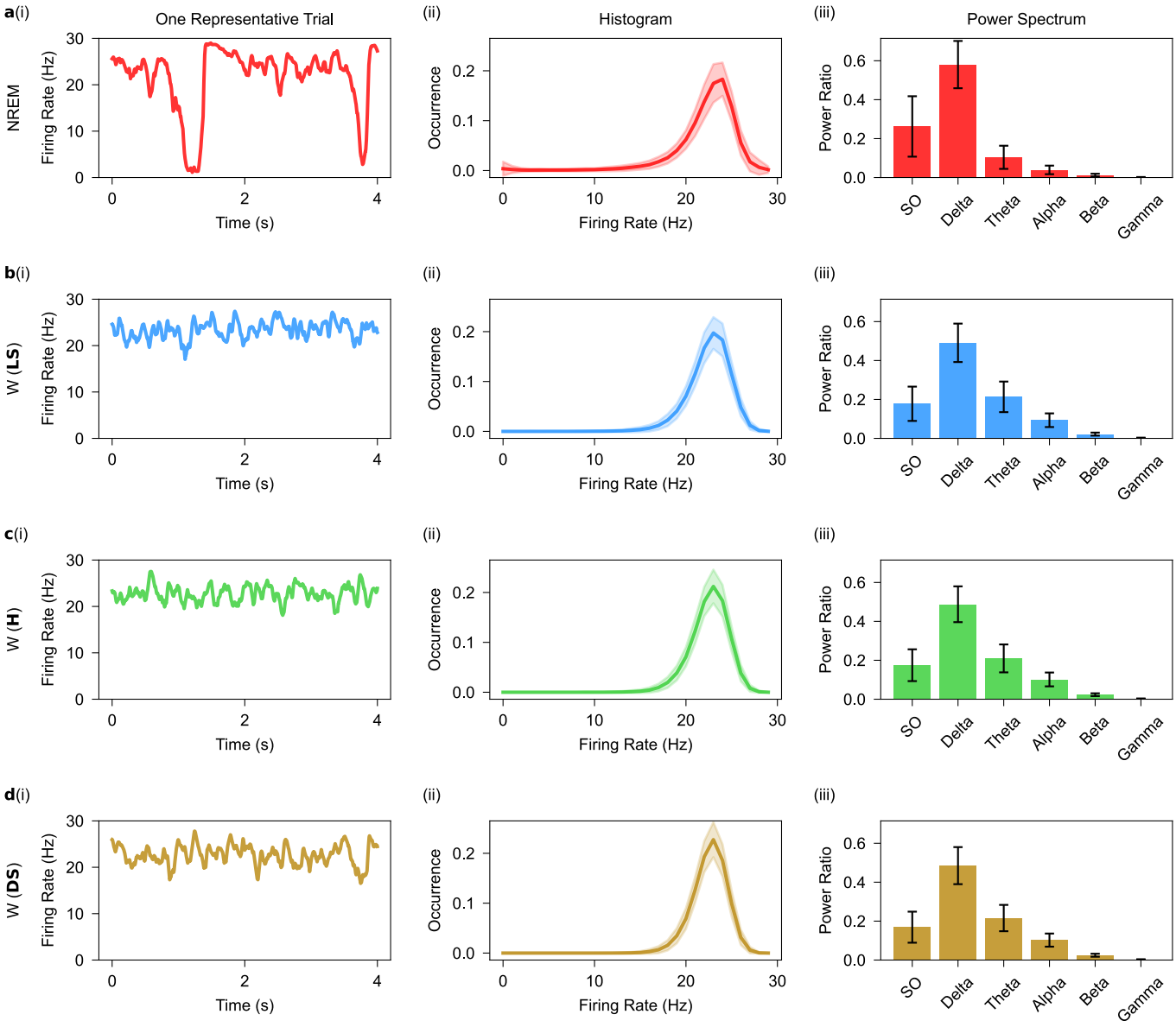

Extended Data Fig. 6. Dynamical features of spontaneous firing activity in the two-cortical-column model. a, Spontaneous firing rate signal for a representative trial (i), the distribution of firing rate signals (ii), and the power spectrum of signals (iii) when there is no intra-synaptic upscaling ($\beta_{intra} = 1$, $\beta_{inter} = 1$). **b**, **c**, and **d**, As in **a**, but for when synaptic upscaling is local-selective (LS: $\beta_{intra} = 4$, $\beta_{inter} = 2$), homogeneous (H: $\beta_{intra} = 4$, $\beta_{inter} = 4$), and distance-selective upscaling (DS: $\beta_{intra} = 4$, $\beta_{inter} = 6$), respectively. The dynamical features of spontaneous firing activity in the two-cortical-column model shift from NREM sleep to wakefulness for all synaptic upscaling combinations (not shown here). Shaded area and Error bar correspond to standard deviation over 500 trials.

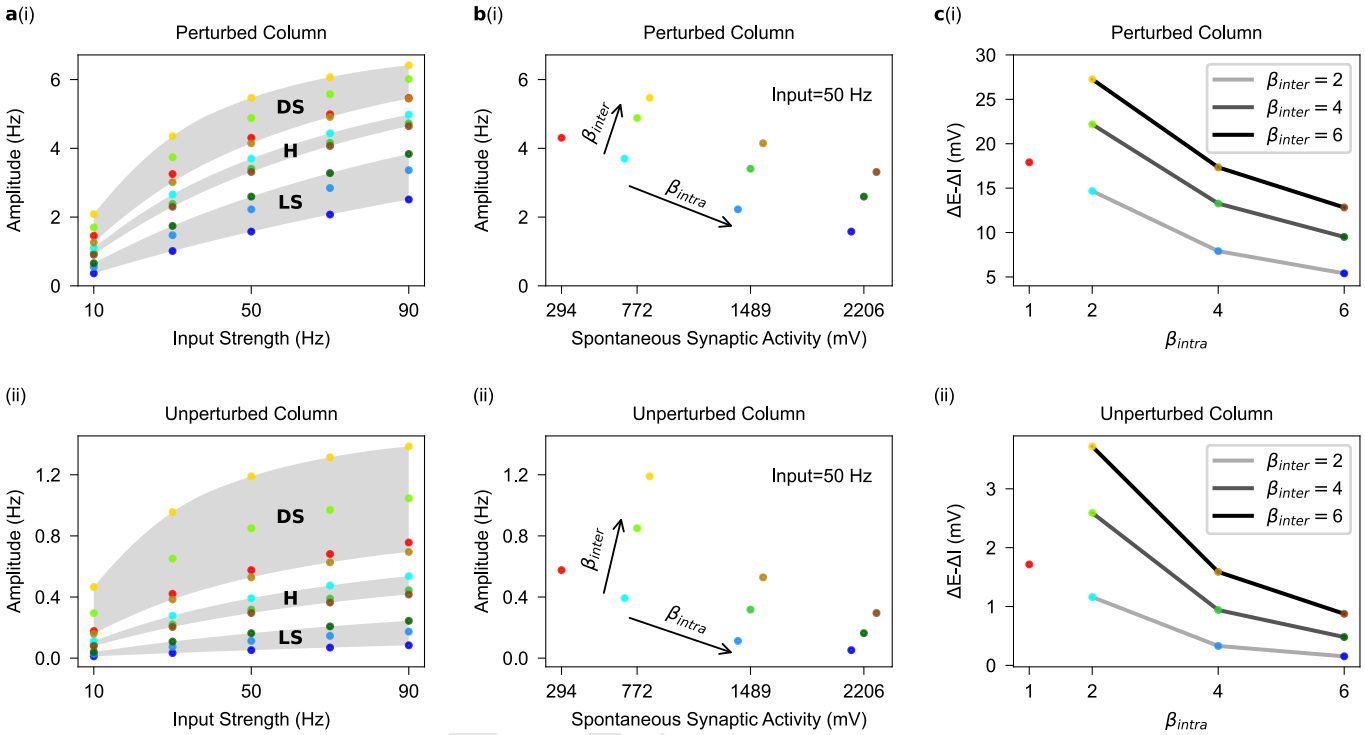

Extended Data Fig. 7. Effect of intra- and inter-synaptic upscaling on the response of two-cortical-column model to inputs. a, The amplitude of evoked responses to inputs in the perturbed (i) and unperturbed cortical column (ii) during wakefulness enhances as synaptic upscaling transition from local-selective (LS) towards distance-selective (DS) upscaling. **b**, Increasing spontaneous synaptic activity ($|E| + |I|$) results in decreasing the amplitude of evoked responses when input strength is 50Hz in the perturbed (i) and unperturbed cortical column (ii). Note that This holds true for other values of input strength (not shown here). Note that inter-synaptic upscaling increases the spontaneous synaptic activity as it is implicated in the dynamics in the two-cortical-column model. **c**, Inter-synaptic upscaling increases the net evoked synaptic current ($\Delta E - \Delta I$), as opposed to when intra-synaptic upscaling increases during wakefulness in the perturbed (i) and unperturbed cortical column (ii).

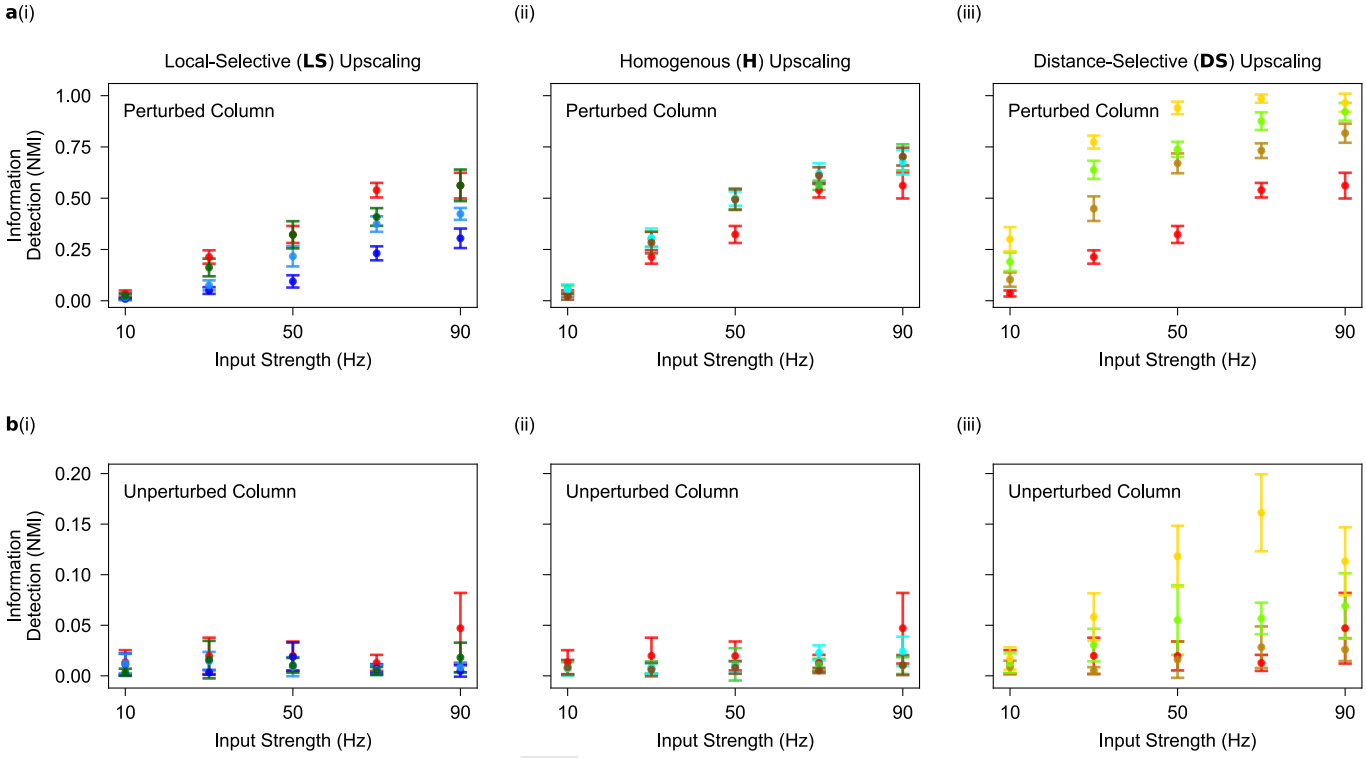

Extended Data Fig. 8. Information detection in the two-cortical-column model. a, Information detection for inputs with increasing input strength in the perturbed cortical column during NREM sleep and wakefulness, when synaptic upscaling in wakefulness is local-selective (i), homogeneous (ii) and distance-selective upscaling (iii). **b**, As in **a**, but for the unperturbed cortical column. Error bar corresponds to 95% confidence interval over 10 performance estimate of the K-means clustering algorithms.

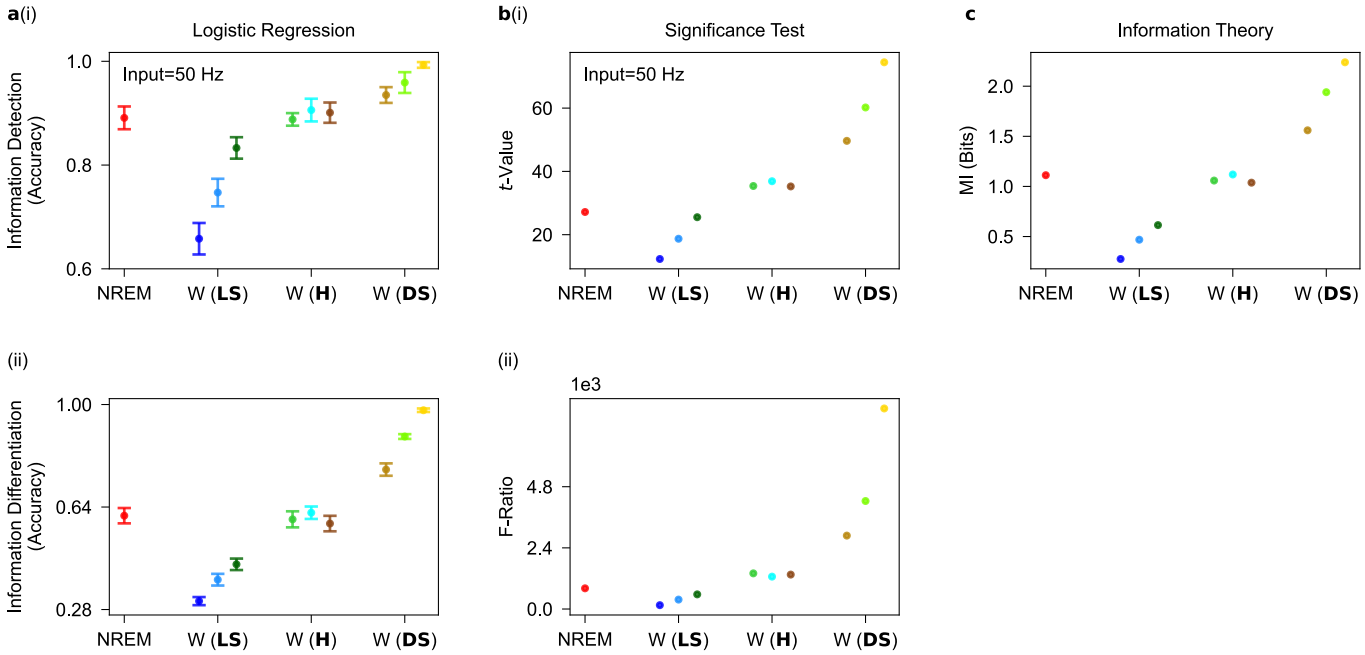

Extended Data Fig. 9. Robustness of the computational results. Figures pertain to analysis of evoked firing responses in the perturbed cortical column in the two-cortical-column model. **a**, Information detection for when input strength is 50Hz (i) and information differentiation (ii) when logistic classification algorithms (Methods) are employed. Error bar corresponds to 95% confidence interval over 10 performance estimate of the logistic classification algorithms. Logistic classification algorithms qualitatively replicate the results obtained using K-means clustering algorithms (Fig. 5**a**). **b**, Implementing significance tests (Methods) such as student t-test (i) and Analysis of variance (ii) qualitatively replicate the results obtain by machine learning techniques pertaining to information detection and information differentiation. **c**, Implementing information theory (Methods) manifests that the mutual information between the distribution of evoked responses at input offset and the distribution of inputs increases as synaptic upscaling transitions from local-selective (LS) to distance-selective (DS) upscaling during wakefulness.

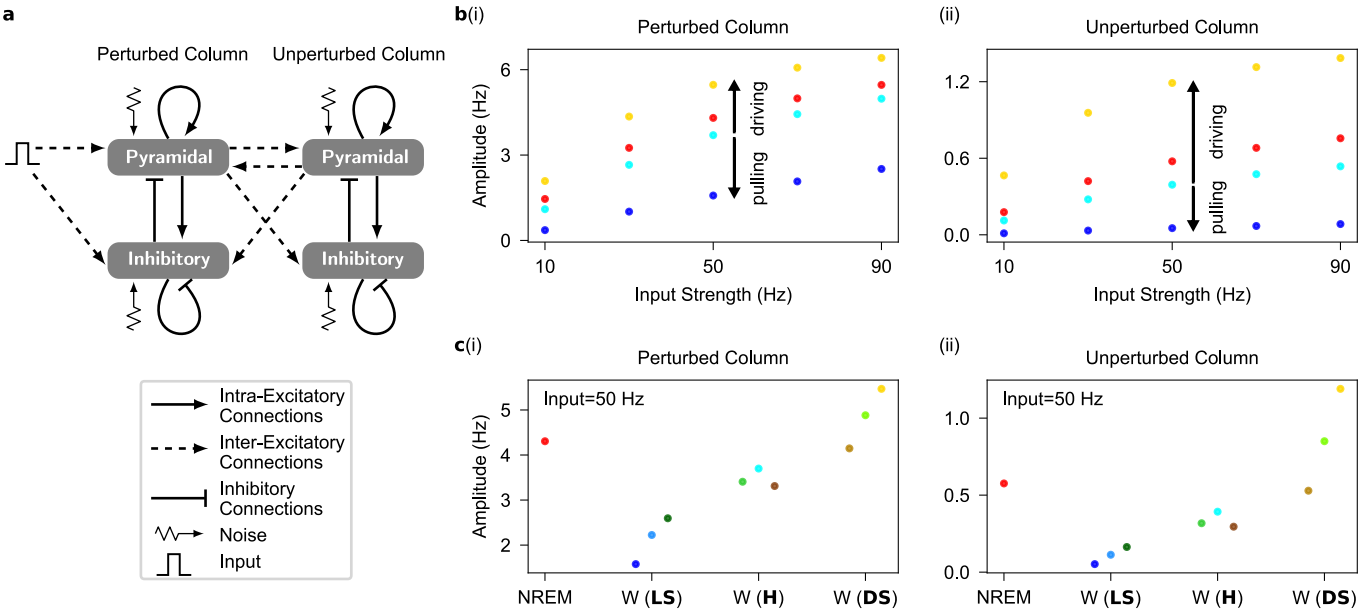
a
Perturbed Column
Unperturbed Column
Pyramidal
Pyramidal
Inhibitory
Inhibitory
Intra-Excitatory Connections
Inter-Excitatory Connections
Inhibitory Connections
Noise
Input
b(i)
Perturbed Column
Amplitude (Hz)
Input Strength (Hz)
driving
pulling
(ii)
Unperturbed Column
Input Strength (Hz)
driving
pulling
c(i)
Perturbed Column
Input=50 Hz
Amplitude (Hz)
NREM
W (LS)
W (H)
W (DS)
(ii)
Unperturbed Column
Input=50 Hz
NREM
W (LS)
W (H)
W (DS)

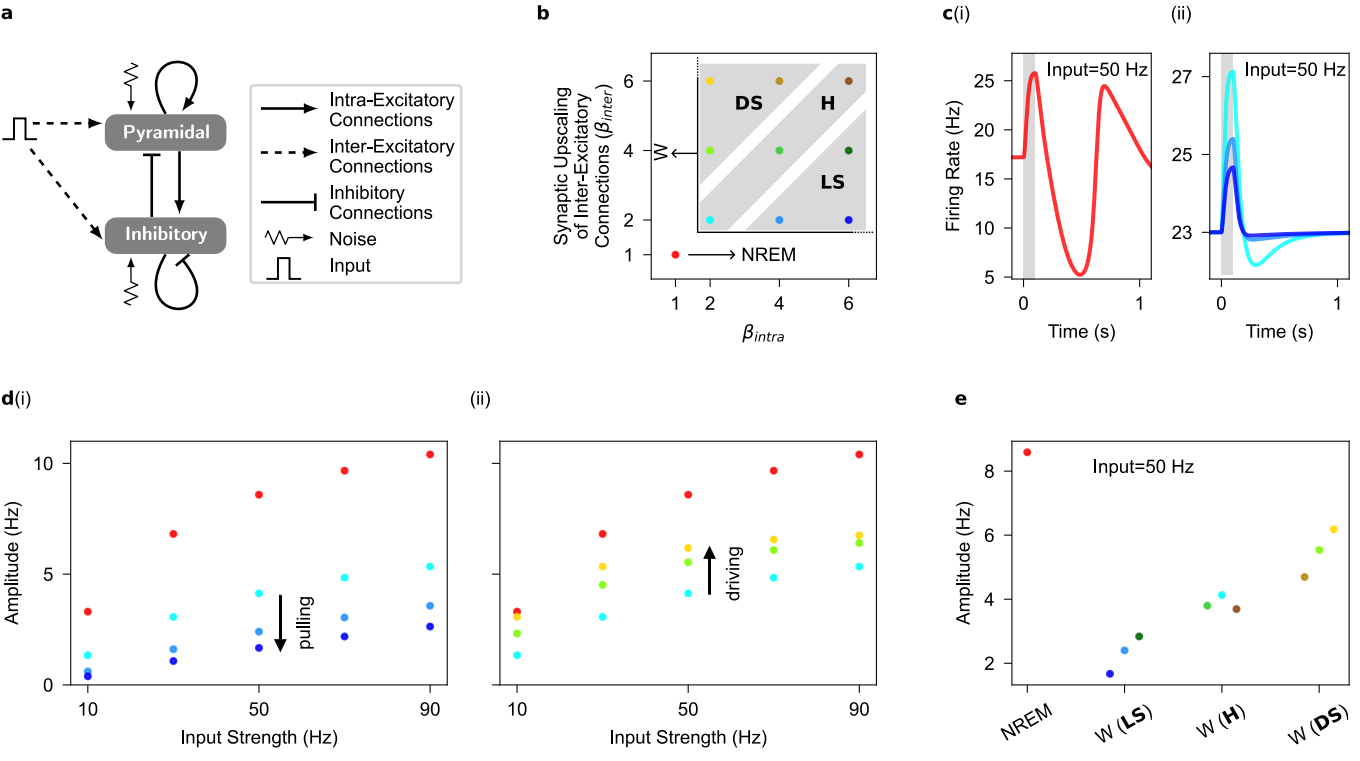
a
Pyramidal
Inhibitory
Intra-Excitatory Connections
Inter-Excitatory Connections
Inhibitory Connections
Noise
Input
b
Synaptic Upscaling of Inter-Excitatory Connections (β_{inter})
β_{intra}
DS
H
LS
W
NREM
c(i)
(ii)
Input=50 Hz
Firing Rate (Hz)
Time (s)
d(i)
(ii)
Amplitude (Hz)
Input Strength (Hz)
pulling
driving
e
Input=50 Hz
Amplitude (Hz)
NREM
W (LS)
W (H)
W (DS)

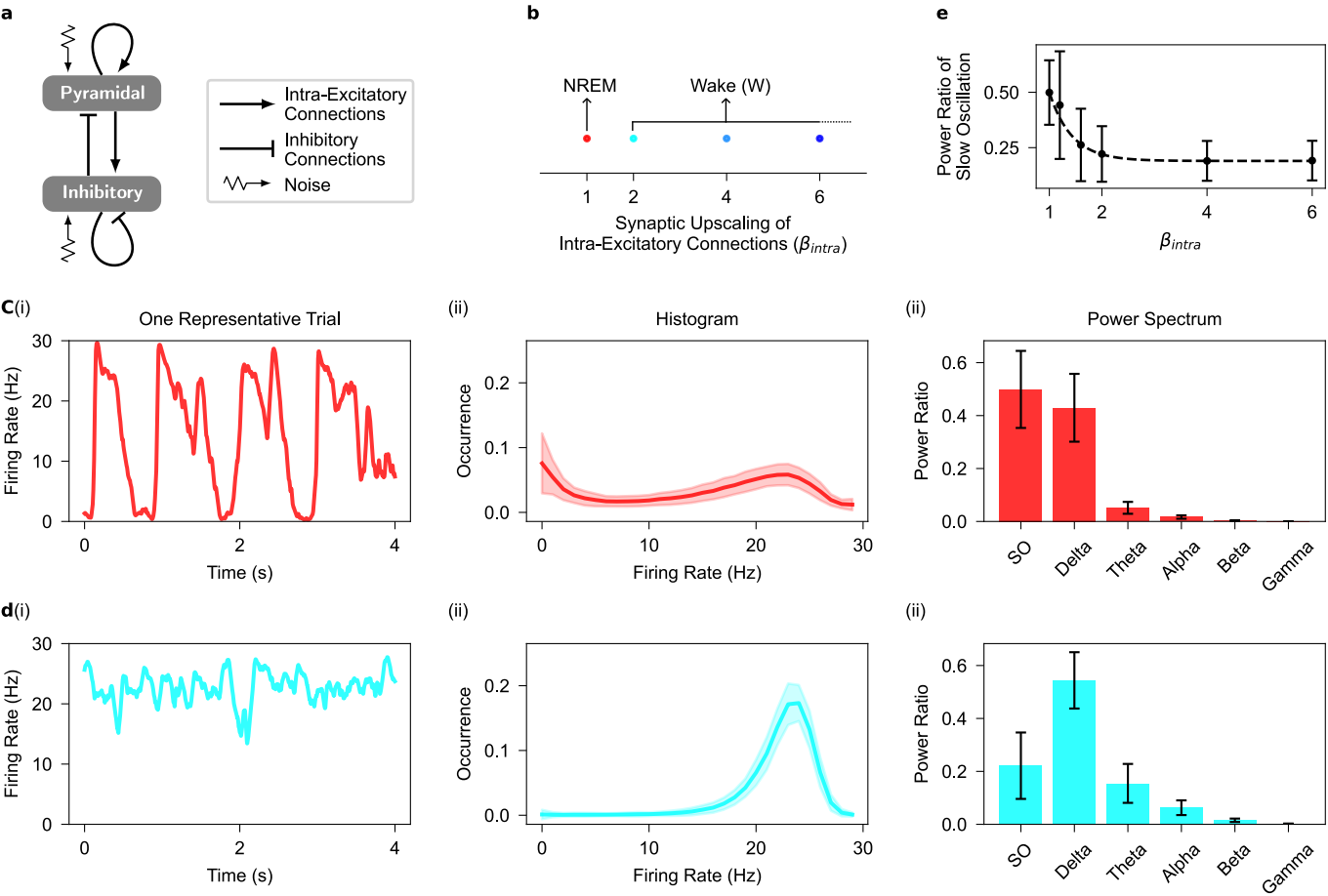
a
Pyramidal
Inhibitory
Intra-Excitatory Connections
Inhibitory Connections
Noise
b
NREM
Wake (W)
1
2
4
6
Synaptic Upscaling of Intra-Excitatory Connections (β_{intra})
e
Power Ratio of Slow Oscillation
0.50
0.25
1
2
4
6
β_{intra}
c(i)
One Representative Trial
Firing Rate (Hz)
Time (s)
(ii)
Histogram
Occurrence
Firing Rate (Hz)
(ii)
Power Spectrum
Power Ratio
SO
Delta
Theta
Alpha
Beta
Gamma
d(i)
Firing Rate (Hz)
Time (s)
(ii)
Occurrence
Firing Rate (Hz)
(ii)
Power Ratio
SO
Delta
Theta
Alpha
Beta
Gamma

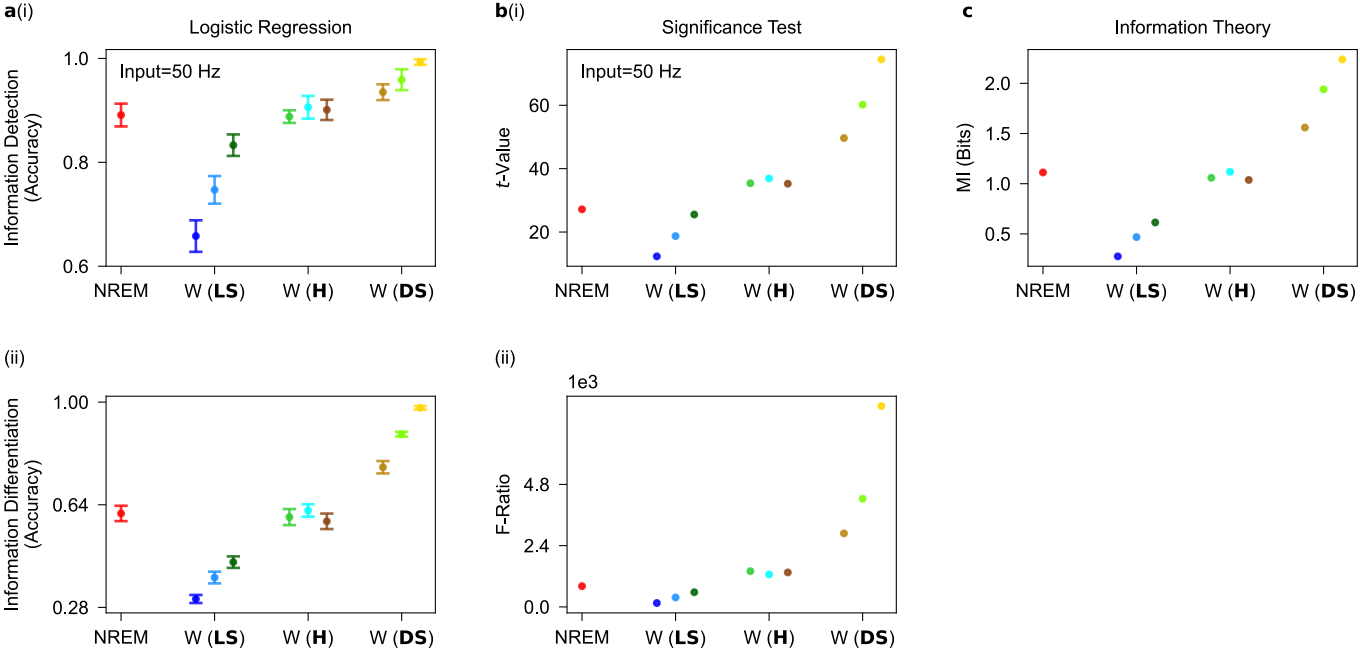
a(i)
Logistic Regression
Input=50 Hz
Information Detection (Accuracy)
1.0
0.8
0.6
NREM
W (LS)
W (H)
W (DS)
b(i)
Significance Test
Input=50 Hz
t-Value
60
40
20
c
Information Theory
MI (Bits)
2.0
1.5
1.0
0.5
(ii)
Information Differentiation (Accuracy)
1.00
0.64
0.28
(ii)
1e3
F-Ratio
4.8
2.4
0.0

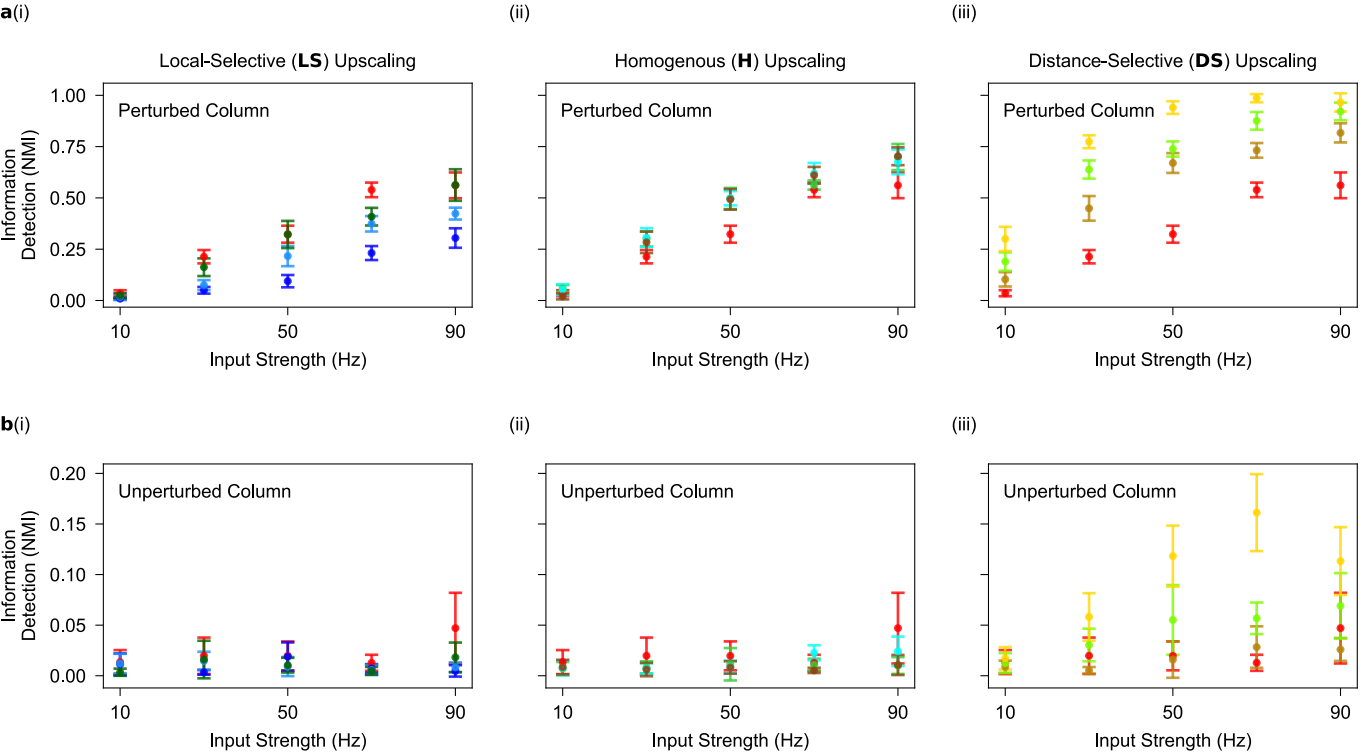
a(i)
(ii)
(iii)
Local-Selective (LS) Upscaling
Homogenous (H) Upscaling
Distance-Selective (DS) Upscaling
Perturbed Column
Information Detection (NMI)
1.00
0.75
0.50
0.25
0.00
10
50
90
Input Strength (Hz)
b(i)
(ii)
(iii)
Unperturbed Column
0.20
0.15
0.10
0.05
0.00

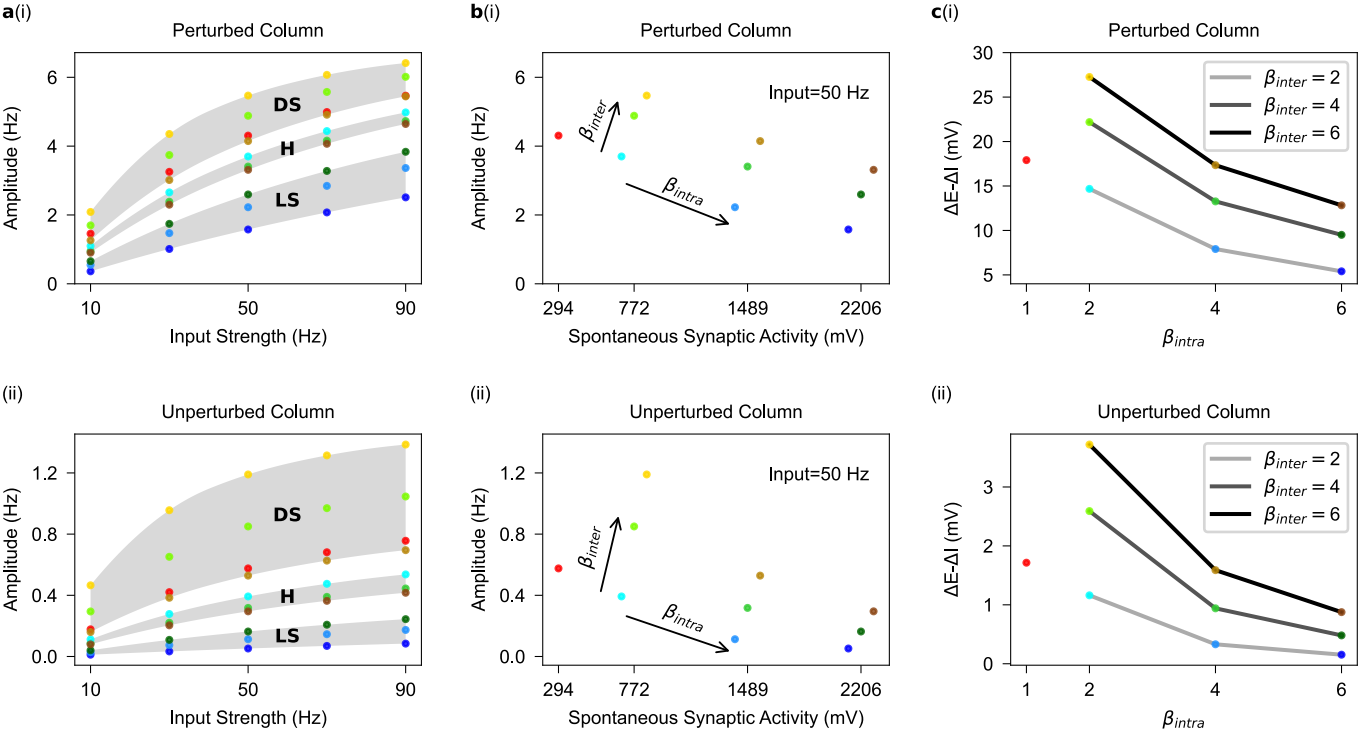
a(i)
Perturbed Column
Amplitude (Hz)
Input Strength (Hz)
DS
H
LS
b(i)
Perturbed Column
Input=50 Hz
β_{inter}
β_{intra}
Amplitude (Hz)
Spontaneous Synaptic Activity (mV)
c(i)
Perturbed Column
$\beta_{inter} = 2$
$\beta_{inter} = 4$
$\beta_{inter} = 6$
ΔE-ΔI (mV)
β_{intra}
(ii)
Unperturbed Column
Amplitude (Hz)
Input Strength (Hz)
DS
H
LS
(ii)
Unperturbed Column
Input=50 Hz
β_{inter}
β_{intra}
Amplitude (Hz)
Spontaneous Synaptic Activity (mV)
(ii)
Unperturbed Column
$\beta_{inter} = 2$
$\beta_{inter} = 4$
$\beta_{inter} = 6$
ΔE-ΔI (mV)
β_{intra}

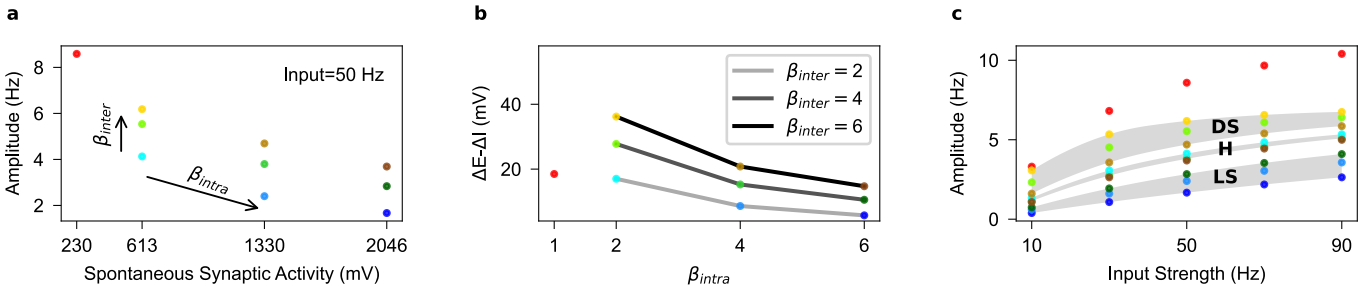
a
Input=50 Hz
Amplitude (Hz)
8
6
4
2
β_{inter}
β_{intra}
230
613
1330
2046
Spontaneous Synaptic Activity (mV)
b
$\beta_{inter} = 2$
$\beta_{inter} = 4$
$\beta_{inter} = 6$
ΔE-ΔI (mV)
40
20
1
2
4
6
β_{intra}
c
Amplitude (Hz)
10
5
0
DS
H
LS
10
50
90
Input Strength (Hz)

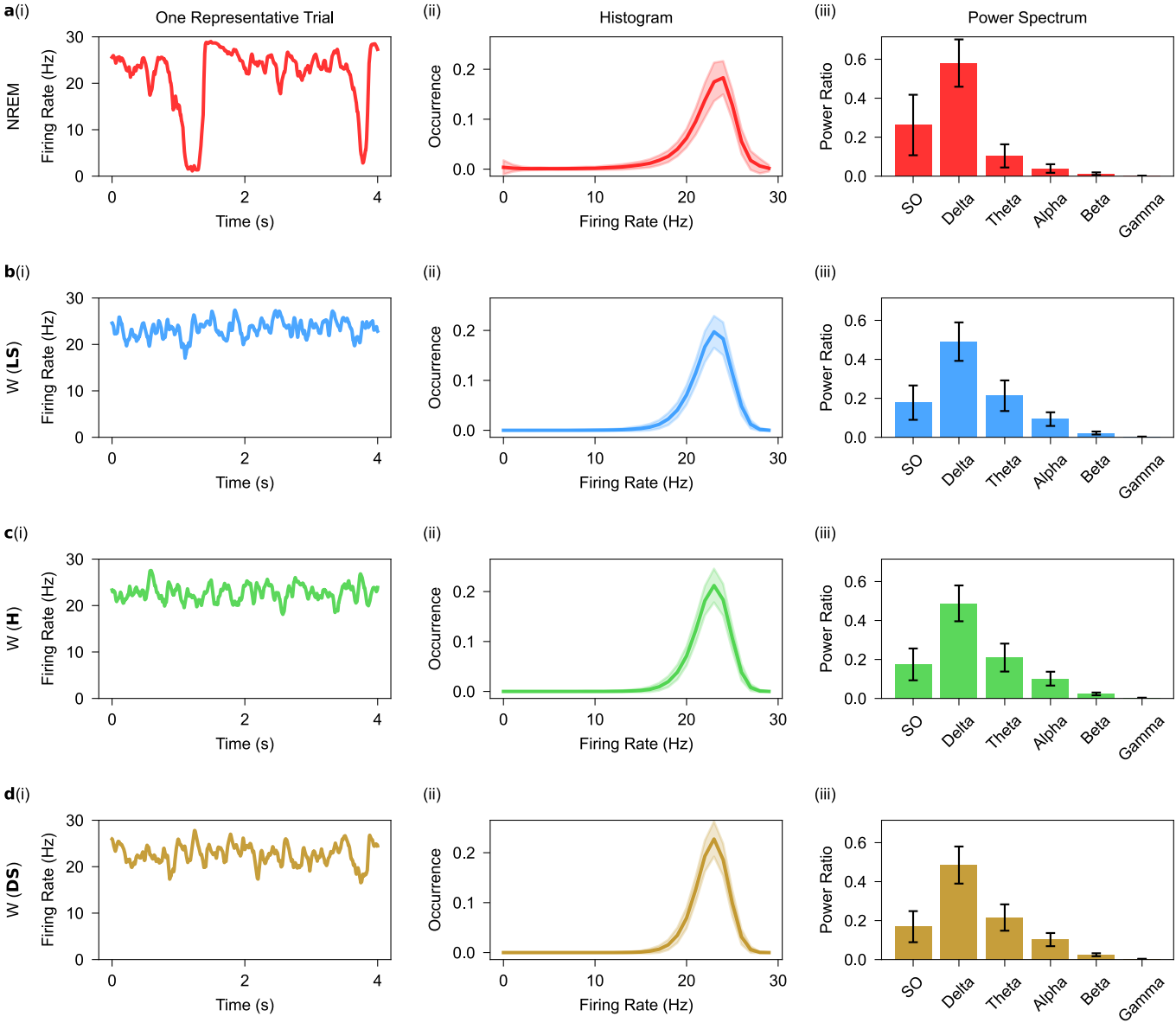
a(i)
One Representative Trial
(ii)
Histogram
(iii)
Power Spectrum
NREM
Firing Rate (Hz)
Time (s)
Occurrence
Firing Rate (Hz)
Power Ratio
SO
Delta
Theta
Alpha
Beta
Gamma
b(i)
W (LS)
c(i)
W (H)
d(i)
W (DS)

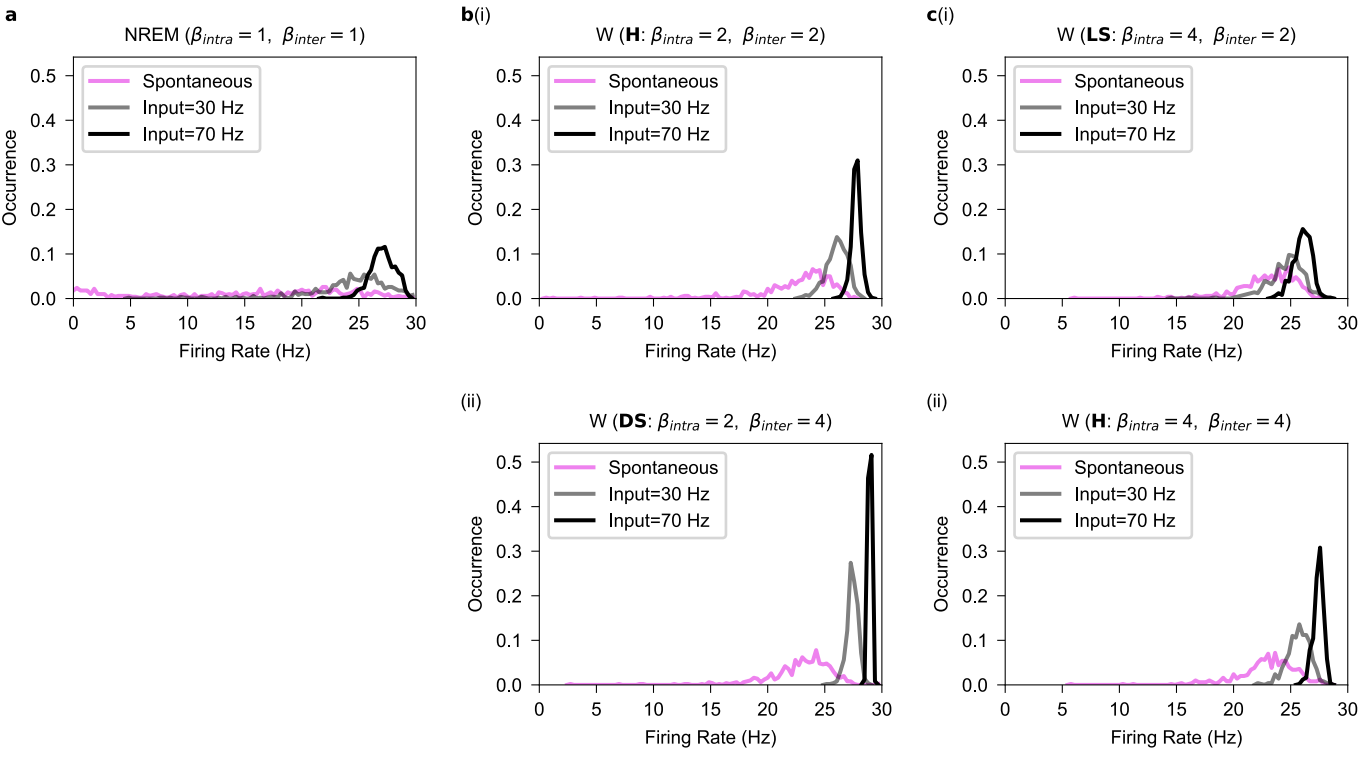
a
NREM ($\beta_{intra} = 1$, $\beta_{inter} = 1$)
b(i)
W (**H**: $\beta_{intra} = 2$, $\beta_{inter} = 2$)
c(i)
W (**LS**: $\beta_{intra} = 4$, $\beta_{inter} = 2$)
(ii)
W (**DS**: $\beta_{intra} = 2$, $\beta_{inter} = 4$)
(ii)
W (**H**: $\beta_{intra} = 4$, $\beta_{inter} = 4$)
Spontaneous
Input=30 Hz
Input=70 Hz
Occurrence
Firing Rate (Hz)
0.0
0.1
0.2
0.3
0.4
0.5
0
5
10
15
20
25
30

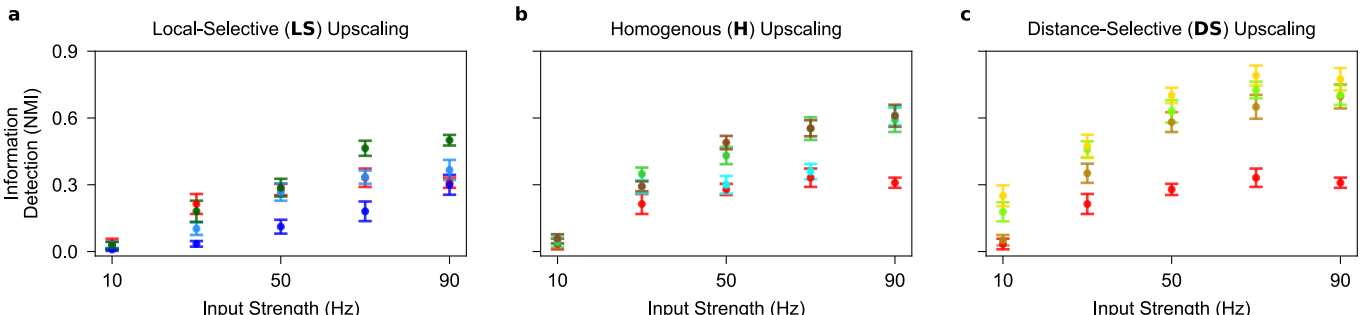
a
Local-Selective (LS) Upscaling
b
Homogenous (H) Upscaling
c
Distance-Selective (DS) Upscaling
Information Detection (NMI)
0.9
0.6
0.3
0.0
10
50
90
Input Strength (Hz)

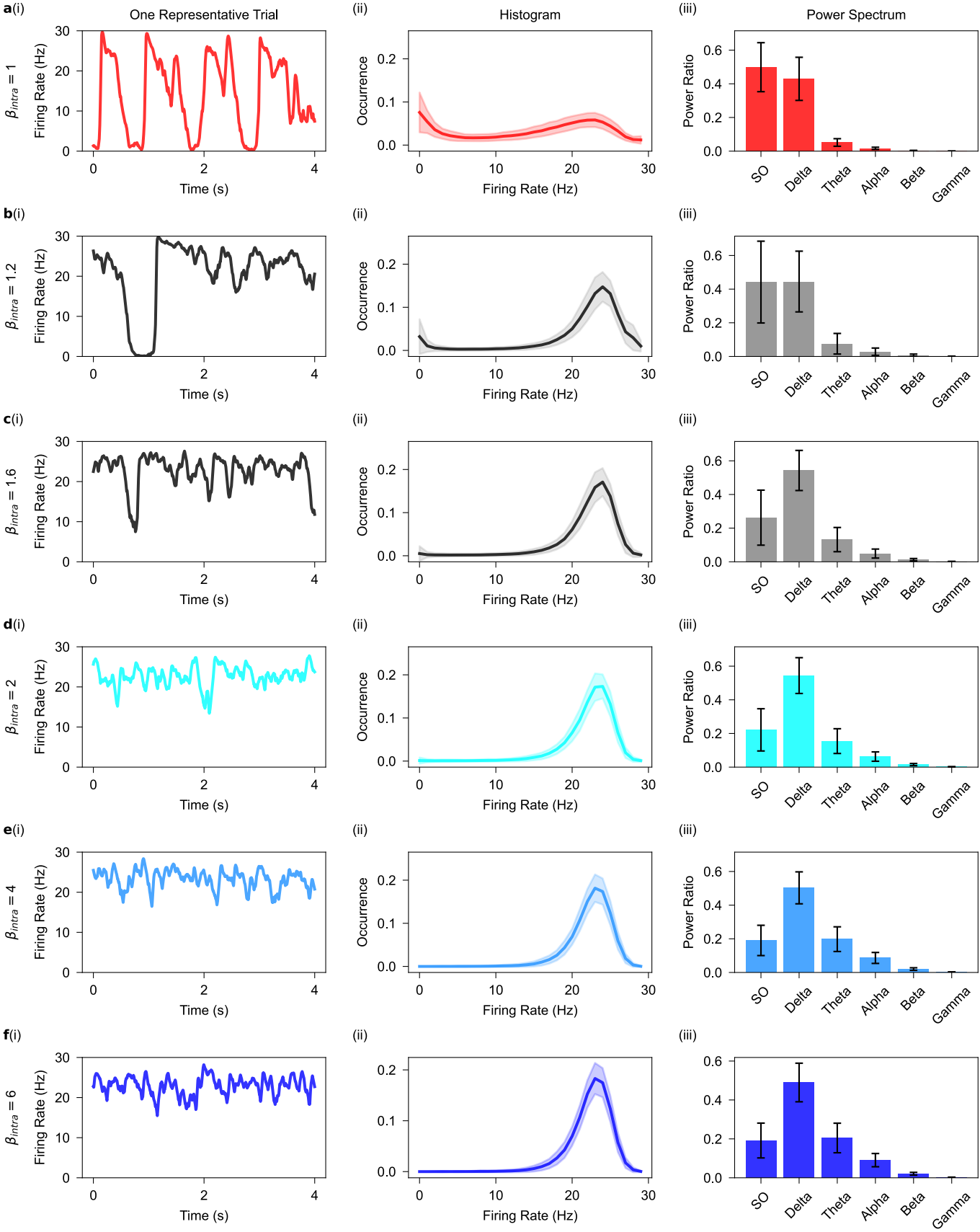
a(i)
One Representative Trial
(ii)
Histogram
(iii)
Power Spectrum
$\beta_{intra} = 1$
b(i)
$\beta_{intra} = 1.2$
c(i)
$\beta_{intra} = 1.6$
d(i)
$\beta_{intra} = 2$
e(i)
$\beta_{intra} = 4$
f(i)
$\beta_{intra} = 6$
Firing Rate (Hz)
Time (s)
Occurrence
Power Ratio
SO
Delta
Theta
Alpha
Beta
Gamma

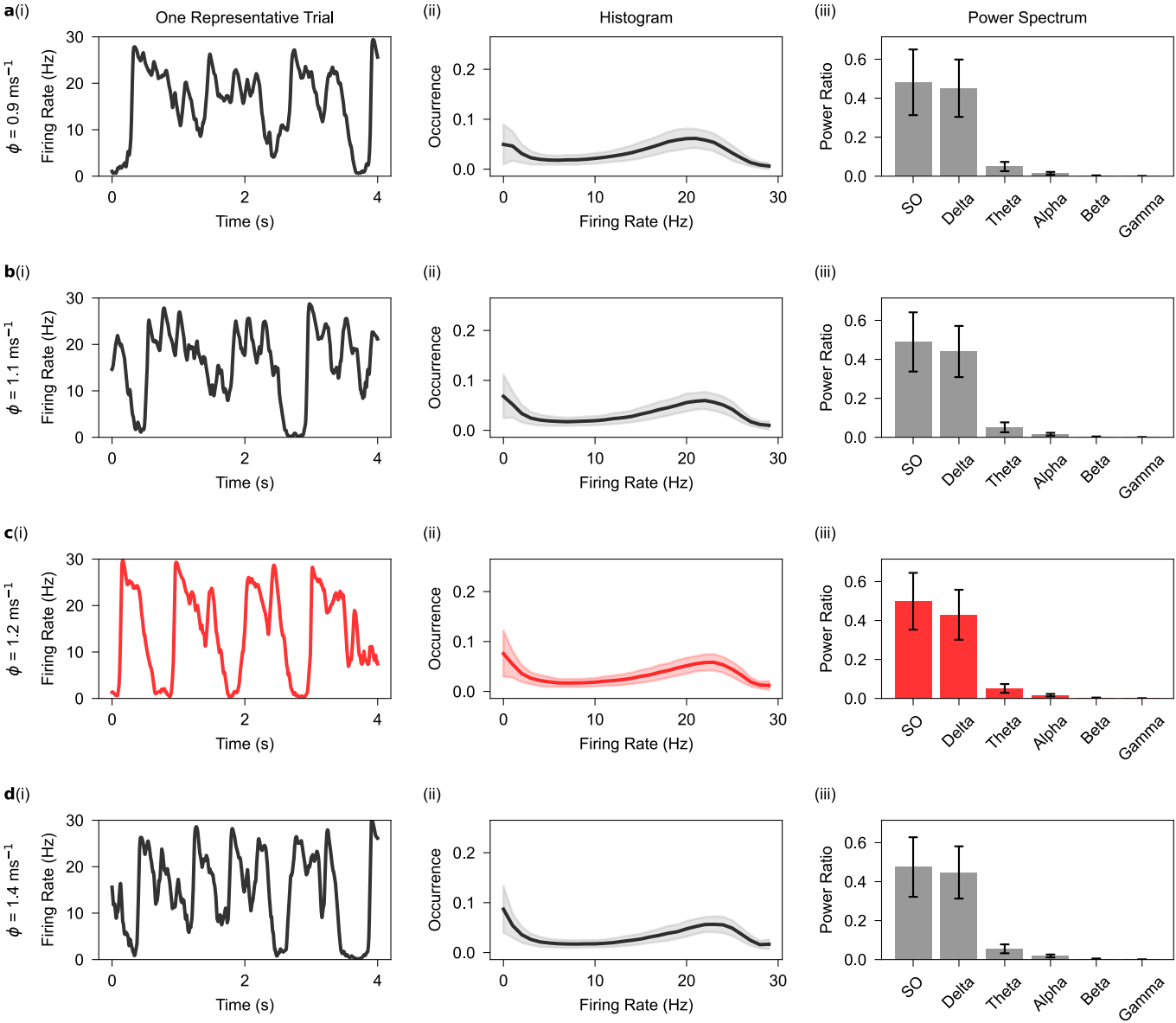
a(i)
One Representative Trial
(ii)
Histogram
(iii)
Power Spectrum
ϕ = 0.9 ms⁻¹
ϕ = 1.1 ms⁻¹
ϕ = 1.2 ms⁻¹
ϕ = 1.4 ms⁻¹
b(i)
c(i)
d(i)
Firing Rate (Hz)
Time (s)
Occurrence
Power Ratio
SO
Delta
Theta
Alpha
Beta
Gamma

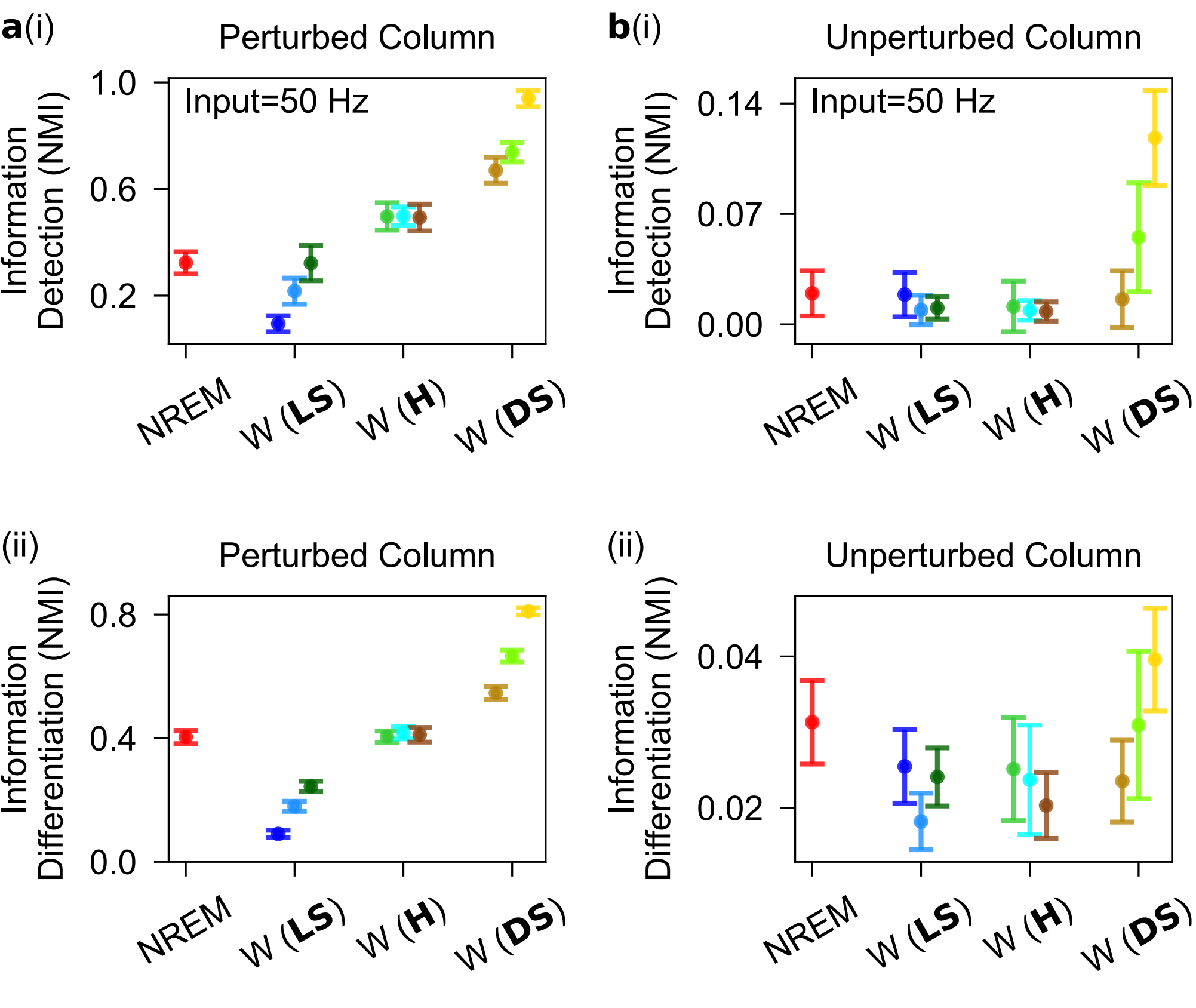
a(i)
Perturbed Column
Input=50 Hz
Information Detection (NMI)
1.0
0.6
0.2
NREM
W (LS)
W (H)
W (DS)
b(i)
Unperturbed Column
Input=50 Hz
Information Detection (NMI)
0.14
0.07
0.00
NREM
W (LS)
W (H)
W (DS)
(ii)
Perturbed Column
Information Differentiation (NMI)
0.8
0.4
0.0
NREM
W (LS)
W (H)
W (DS)
(ii)
Unperturbed Column
Information Differentiation (NMI)
0.04
0.02
NREM
W (LS)
W (H)
W (DS)

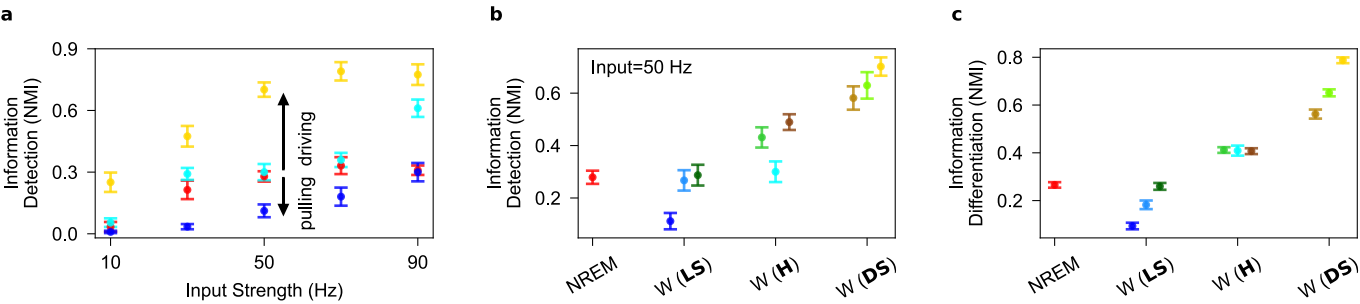
a
Information Detection (NMI)
0.9
0.6
0.3
0.0
10
50
90
Input Strength (Hz)
pulling
driving
b
Input=50 Hz
Information Detection (NMI)
0.6
0.4
0.2
NREM
W (LS)
W (H)
W (DS)
c
Information Differentiation (NMI)
0.8
0.6
0.4
0.2
NREM
W (LS)
W (H)
W (DS)